Downloaded from https://academic.oup.com/mnras/article/540/1/1163/8128274 by guest on 27 October 2025

Evidence for universal gas depletion in a sample of 41 luminous Type 1 quasars at $z \sim 2$

S. J. Molyneux ¹, ¹* M. Banerji ¹, ¹ M. J. Temple ¹, ² M. Aravena, ³ R. J. Assef, ³ P. Hewett ¹, ⁴ G. C. Jones ¹, ^{5,6} A. Puglisi ¹, ¹ A. L. Rankine ¹, ⁷ C. Ricci, ^{3,8} M. Stepney ¹ and S. Tang ¹

Accepted 2025 May 8. Received 2025 May 6; in original form 2025 March 31

ABSTRACT

We present ALMA CO observations of the molecular gas in a sample of 41 luminous unobscured quasars at $z\sim 2$ from the Sloan Digital Sky Survey (SDSS). 32 targets comprise the main sample observed in CO(3-2), and 9 targets have archival ALMA data of CO(3-2), CO(4-3), and CO(7-6). All quasars have rest-ultraviolet to optical spectra tracing ionized gas in the broad line region (e.g. C IV) and the narrow line region (e.g. [O III]) and they cover the full range of outflow properties in the SDSS quasar population at these redshifts. 15 out of the 32 quasars in the main sample are detected in CO(3-2) and five out of the nine archival quasars are also detected in CO. The median gas mass for all 20 CO-detected quasars is $8.0\pm1.5\times10^9~\rm M_{\odot}$ with a median $M_{\rm dyn}$ of $1.4\pm0.9\times10^{11}~\rm M_{\odot}$. We find gas fractions in the range 0.02–0.32, which are generally lower than both inactive galaxies and obscured quasars at similar redshifts. We suggest an evolutionary trend in gas fractions of quasar host galaxies from obscured and gas rich to unobscured and gas poor. We note a tentative correlation between the gas fractions and the broad-line region properties with quasars showing high C IV blueshifts, indicating stronger broad-line region winds, having higher gas fractions. Six of the quasars corresponding to 15 per cent of the sample also show evidence for at least one companion galaxy detected in CO at the same redshift.

Key words: Galaxy: evolution – galaxies: active – quasars: general.

1 INTRODUCTION

Feedback from active galactic nuclei (AGNs) is required to explain our current understanding of galaxy evolution, as it is thought to regulate the observed co-evolution of accreting black holes (BH) and their host galaxies across cosmic time (e.g. Fabian 2012; Cresci & Maiolino 2018). To understand the physical processes by which feedback can impact the host galaxy, we need to characterize the interactions between central supermassive black holes and the host galaxy interstellar medium (ISM) across multiple gas phases (e.g. molecular, ionized, and atomic). This requires observations at different wavelengths and spatial scales.

Studies investigating the properties of the multiphase interstellar medium (ISM) in quasar host galaxies find the presence of kpc-scale outflows in the ionized phase traced by [O III]5007 Å (e.g. Harrison et al. 2014; Carniani et al. 2015; Cresci et al. 2015; Circosta et al. 2018; Kakkad et al. 2020; Scholtz et al. 2020; Vayner et al.

* E-mail: smolyneux.astro@gmail.com

2021; Concas et al. 2022; Wylezalek et al. 2022) and also in the molecular phase traced by carbon monoxide (CO; e.g. Cicone et al. 2012; Feruglio et al. 2015; Brusa et al. 2018; Bischetti et al. 2019; Longinotti et al. 2023). These multiphase outflows have been sen to correlate with AGN properties such as luminosity (e.g. Mullaney et al. 2013; Fiore et al. 2017) and the presence of radio jets (e.g. Molyneux, Harrison & Jarvis 2019). These observations show the ability of AGN activity to expel the star-forming ISM and would suggest that AGNs can have an impact on the gas reservoirs of their host galaxies. The molecular phase of the ISM is an important consideration, since this gas is redistributed to promote star formation activity and fuel BH growth (e.g. McKee & Ostriker 2007; Carilli & Walter 2013; Vito et al. 2014; Tacconi, Genzel & Sternberg 2020), and therefore plays a critical role in galaxy evolution.

To analyse the molecular phase of the ISM, CO is routinely observed, which can provide an instantaneous measure of the current available fuel for star formation (Bolatto, Wolfire & Leroy 2013). We can trace an impact by AGN activity by observing the gas fractions (the ratio of the gas mass to the stellar mass). Indeed, some luminous quasars at high redshift (z > 2) that are driving powerful

© 2025 The Author(s).

¹School of Physics and Astronomy, University of Southampton, Southampton SO17 1BJ, UK

²Centre for Extragalactic Astronomy, Department of Physics, Durham University, South Road, Durham DH1 3LE, UK

³Instituto de Estudios Astrofísicos, Facultad de Ingeniería y Ciencias, Universidad Diego Portales, Avenida Ejercito Libertador 441, Santiago 8370191, Chile

⁴Institute of Astronomy, University of Cambridge, Madingley Road, Cambridge CB3 0HA, UK

⁵Kavli Institute for Cosmology, University of Cambridge, Madingley Road, Cambridge CB3 0HA, UK

⁶Cavendish Laboratory, University of Cambridge, 19 JJ Thomson Avenue, Cambridge CB3 0HE, UK

⁷Institute for Astronomy, University of Edinburgh, Royal Observatory, Edinburgh EH9 3HJ, UK

⁸Kavli Institute for Astronomy and Astrophysics, Peking University, Beijing 100871, China

winds show depleted gas reservoirs compared to their non-AGN counterparts (e.g. Bischetti et al. 2021; Circosta et al. 2021; Bertola et al. 2024). However, AGNs at lower redshifts (z < 0.3) are also routinely observed to be hosted in gas-rich, star-forming galaxies, with no signs of a depleted molecular gas reservoir compared to non-AGNs (e.g. Saintonge et al. 2017; Jarvis et al. 2020; Lamperti et al. 2020; Shangguan et al. 2020; Koss et al. 2021). Simulations also support the picture from the local Universe with AGNs having higher gas fractions than non-AGNs, and residing in gas-rich, starforming galaxies (Piotrowska et al. 2022; Ward et al. 2022). These results indicate that powerful AGNs/quasars do have the ability to have a significant impact on the global properties of their host galaxies, but that gas-rich environments are also needed to fuel the most powerful quasars. The molecular gas properties of AGNs also depend on redshift, luminosity, and obscuration (e.g. Perna et al. 2018; Banerji et al. 2021; Bischetti et al. 2021; Circosta et al. 2021; Sun et al. 2024).

In addition to multiphase outflows on kpc scales, luminous guasars also show evidence of outflows on sub-parsec scales. High ionization emission lines such as C IV 1550 Å that show strong asymmetries to the blue, can be indicative of radiatively driven accretion disc winds in the quasar broad line region (BLR; e.g. Richards et al. 2011; Rankine et al. 2020; Stepney et al. 2023). There are established correlations between the prevalence of these strong winds and the ultraviolet (UV) SEDs of quasars (e.g. Vietri et al. 2020; Temple et al. 2023). For example, the He II 1640 Å emission line provides a probe of the hardness of the ionizing SED (Leighly & Moore 2004; Baskin, Laor & Hamann 2013, 2015) and is also correlated to C IV blueshift with quasars that have softer ionizing SEDs driving stronger outflows (Temple et al. 2023). Quasars with and without broad absorption lines (BALs), which are considered a more direct probe of high-velocity winds, also appear to have very similar emission line properties (Rankine et al. 2020) as well as showing a similar relationship between emission line morphology and ionizing SED as the non-BAL population (Temple et al. 2023).

To test whether there is any link between the rest-frame UV spectra and the wider, global properties of the host galaxy, we can study correlations between the UV spectra and the global ISM properties. As discussed before, [O III] is a useful tracer of the ionized phase of the ISM in the narrow-line region (NLR) and therefore a good emission line to use in these analysis. Winds from the accretion disc, traced by the blueshift of CIV, have been shown to correlate with the velocity of winds in the quasar NLR as traced by [O III] (Coatman et al. 2019; Vietri et al. 2020; Temple et al. 2024). Since the [O III] emission traces outflows on larger scales than C IV, a correlation in the kinematics of these two ionized gas tracers is consistent with the scenario that quasar disc winds could be responsible for the impact observed on the ISM at kiloparsec scales. An interesting avenue of research is therefore to test whether any such link can be made to the molecular gas (CO) and make comparisons to ionized outflows from the NLR ([O III]) and the BLR (C IV).

In addition to the properties of the ISM host galaxy, there are also unanswered questions relating to the environments of luminous high-z quasars and whether or not they reside in over dense regions. Several previous studies have identified companion galaxies to quasar host galaxies at z=2-6 either in individual systems (Ivison et al. 2008; Salomé et al. 2012; Banerji et al. 2017; Decarli et al. 2017; Fogasy et al. 2017; Trakhtenbrot et al. 2017; Neeleman et al. 2019; Fogasy et al. 2020; Banerji et al. 2021; Stacey & Arrigoni Battaia 2022; Li et al. 2023). The samples studied are, however, small, which motivates work across larger samples to determine whether overdensities are prevalent across all luminous AGNs and quasars.

In this work, we present a comprehensive study of the molecular gas properties of 41 quasars at $z\sim2$, traced by CO observations with ALMA. The sample has already been well studied, with analysis of the rest-frame UV spectra (Rankine et al. 2020; Temple et al. 2023) and rest-frame optical spectra (Temple et al. 2024). These detailed spectroscopic characterizations make the sample unique, with information about the ionized gas across different spatial scales. We can now explore the relationship between the sub-parsec scale nuclear region (traced by the rest-frame UV spectra) and NLR ([O III]) to the global molecular ISM – traced by CO. We compare our results to samples of star-forming galaxies, AGNs, and quasars across the redshift range 0–5 from the literature.

In Section 2, we introduce the sample of quasars and the data used in this work. In Section 3, we describe the analysis techniques used to study the molecular gas and dust continuum. We calculate gas masses and gas fractions and compare to other populations in the literature to place our findings in context. In Section 4, we discuss our findings and our final conclusions are presented in Section 5.

We adopt a flat Lambda cold dark matter (CDM) cosmology with parameters: $H_0 = 70 \, \mathrm{km \ s^{-1} \ Mpc^{-1}}$, $\Omega_M = 0.3$, and $\Omega_{\Lambda} = 0.7$ throughout.

2 OBSERVATIONS AND ANCILLARY DATA

2.1 Sample selection

The quasars presented here were selected from a larger parent sample of \sim 144k quasars from the Sloan Digital Sky Survey Data Release 14 (SDSS DR14) at $1.6 \lesssim z \lesssim 3.5$ where the rest-frame UV spectra have been analysed in detail to constrain their accretion and outflow properties (Rankine et al. 2020; Temple et al. 2023). We restricted the sample to the subset of quasars with rest-frame optical spectra covering [O III] from either the Gemini GNIRS Distant Quasar Survey (Matthews et al. 2021) or the compilation of Coatman et al. (2019). The [O III] data enable us to constrain outflows on larger scales in the quasar NLR, and relate this to the molecular gas properties. To ensure high-quality [O III] measurements we restrict the parent sample to magnitudes $i_{\rm AB} < 19.1$ and a limited range in redshift of $2.2 \lesssim z \lesssim 2.4$.

To generate a sample to target with ALMA, we then identified a subset of 50 of these quasars with rest-UV and rest-optical spectroscopy which cover the full range in C_{IV} blueshifts and equivalent widths as the parent SDSS sample. Due to the known correlations between C IV and [O III] emission line properties (Vietri et al. 2018; Coatman et al. 2019; Temple et al. 2024) this also results in a range of [O III] line widths and equivalent widths. Our sample selection therefore allows us to investigate how the molecular gas properties of quasar host galaxies depend on the outflow properties measured from their rest-frame UV and optical spectra. Of these 50 targets, CO(3-2) was observed in 32 quasars during ALMA Cycle 8, which therefore comprise the main sample of quasars presented here. Our sample includes 21 BAL quasars, allowing us to look at differences in molecular gas properties between BALs and non-BALs. The sample deliberately covers a limited range in luminosity and black hole mass [median $log_{10}(L_{3000}/erg s^{-1}) = 46.7$ and $\log_{10}(M_{\rm BH}/\rm M_{\odot}) = 9.48$; Temple et al. (2023), allowing us to explicitly test the dependence of molecular gas properties on outflow properties measured from the rest-UV and optical spectra.

In addition to the main sample of 32 quasars, we identified another 9 targets using the ALminer tool (Ahmadi & Hacar 2023) to match all quasars from the parent Rankine et al. (2020) sample with the ALMA archival data base, using a matching radius of 0.75 arcmin

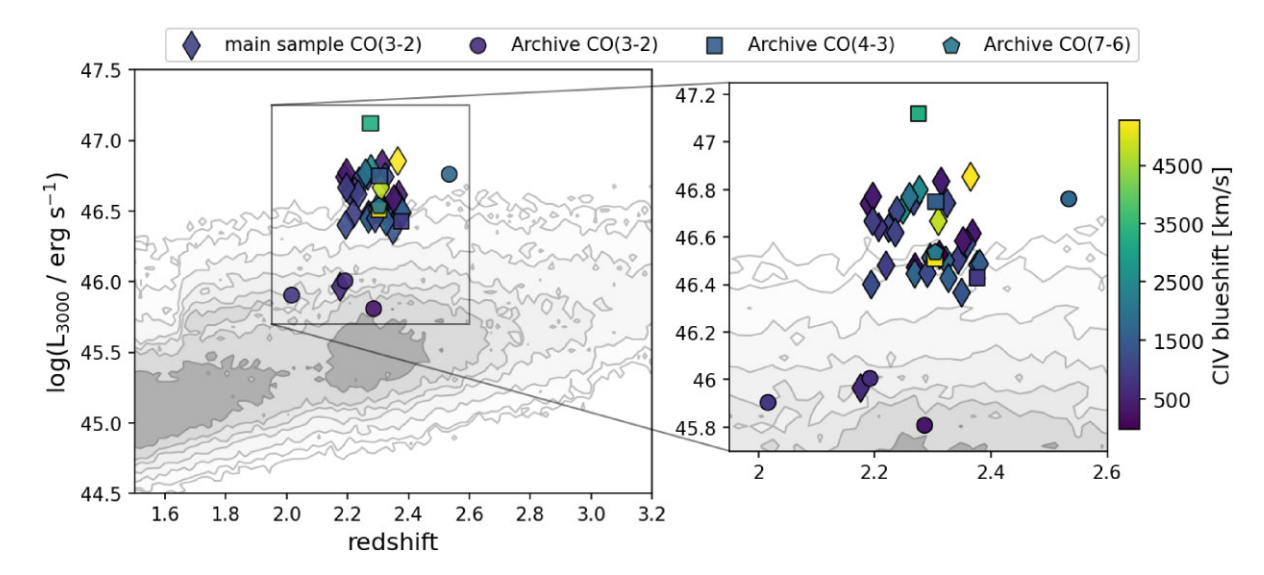


Figure 1. Here we present the sample selection for the quasars presented in this work. We plot the sample in the redshift and 3000 Å luminosity parameter space, coloured by the C IV blueshifts. The grey contours/shaded region indicate the full distribution of SDSS DR16 quasars from Rankine et al. (2020) and Temple et al. (2023). Diamonds indicate the main sample from ALMA project ID 2021.1.00393.S (PI: M. Temple). We also show archival ALMA data utilized within this work, with CO(3-2) data presented as circles, CO(4-3) data presented as squares, and CO(7-6) data presented as hexagons. For a full description of the sample selection, see Section 2.1.

(corresponding to $\sim 360\,\mathrm{kpc}$, the primary beam of ALMA for the main sample presented here). These archival data have the same selection criteria as the main sample and are included to increase the sample size. These additional targets are referred to as the archival sample and include observations of the CO(3-2) emission of 4 targets [project IDs, 2013.1.01262.S (PI: J. Prochaska), 2016.1.00798.S (PI: V. Mainieri), 2017.1.01676.S (PI: C. Ross)], CO(4-3) emission of 4 targets [project ID 2019.1.01251.S (PI: B. Emonts) (see Li et al. 2023)], and CO(7-6) in 1 target [project 2018.1.00583.S (PI. F. Hamann)]. The redshift and luminosity for the sample colour coded by their C IV blueshift is presented in Fig. 1.

2.2 ALMA observations

We used 12-m array ALMA band 3 to observe the molecular gas emission traced by the CO(3–2) transition in a sample of 32 luminous quasars at 2.2 < z < 2.4. These observations were taken in 2022 January–September, observed under the project ID 2021.1.00393.S (PI: M. Temple), in the configurations C43-1, C43-2, C43-3, and C43-4. We refer to these targets as the main sample of this work. Further details of the observations can be found in Table 1.

We observed the CO(3-2) emission line down to a uniform sensitivity limit of $\sim 0.5 \mathrm{mJy}$ per 33 km s $^{-1}$ bin width (see Table 1) and at a resolution of 1–3 arcsec, to obtain unresolved observations of the total molecular gas content. The spectral windows of the observations were aligned to cover the CO(3-2) with one window centred at the expected CO(3-2) frequency based on the systemic redshifts calculated for these quasars as described in section 3 of Rankine et al. (2020). Briefly, the redshifts are derived from spectral reconstructions based on a Mean-Field Independent Component Analysis (MFICA) technique applied to spectra with an improved sky-subtraction routine relative to the SDSS pipeline. The redshift estimation routine uses the rest-frame 1600–3000 Å region, which deliberately excludes the C IV emission line which can be significantly blueshifted relative to systemic. This is a key difference relative to the SDSS pipeline redshifts and should result in more

robust systemic redshifts from the UV spectra. More details of the UV redshift estimates can be found in Rankine et al. (2020).

As shown in Table 1, the archival samples (introduced in Section 2.1) reach different sensitivity limits and some also trace different CO transitions compared to the main sample. When analysing correlations between the molecular gas and the UV/optical line properties (Section 3.6), we therefore only use the main sample, which has a uniform sensitivity.

All the data utilized here are the reduced ALMA data products available from the ALMA archive which have been continuum subtracted and primary beam corrected. To make sure these products were reliable, we carried out our own reductions of some of the targets within the sample, namely J2352-0120, J1113 + 1022, and J2239-0047 which covered the full range of beam sizes (1–3 arcsec), allowing us to test whether sources had been resolved. We used the TCLEAN function in CASA to test different reductions with different parameters such as the weighting (natural and briggs with robust -0.5, 0, and 0.5) as well as the cleaning thresholds ranging from 0.5 to 2 times the threshold used to create the original ALMA product. Quantitatively, we identified a variation in the total line flux obtained on the order of < 2 per cent, well within the uncertainties measured.

2.3 Ancillary data

In addition to ALMA observations of CO, all 41 targets possess ancillary multiwavelength data as described below.

2.3.1 Rest frame UV data

For all targets presented in this paper we have rest frame UV spectroscopy obtained from SDSS DR14 (Pâris et al. 2018). For the purposes of this paper we make use of the MFICA reconstructions produced by Rankine et al. (2020), who use the properties of the 1900 Å emission-line blend to place priors on the MFICA component weights, allowing the intrinsic emission-line profile of C IV λ 1549 to be reconstructed even in objects with broad absorption features. For

Table 1. Details of the CO observations including the observed CO line and ALMA project id, the source name, beam size, line rms, observing times ($t_{\rm obs}$), and continuum rms.

Line	Source name	Beam size (arcsec)	Line RMS, $\Delta v = 50 \text{ km s}^{-1}$ (mJy)	$t_{\rm obs}$ (min)	continuum rms (μJy)
		(aresec)	(IIIJy)	(11111)	(μ3γ)
CO(3-2) main sample	J0014 + 0912	1.124	0.31	55.4	13.8
ALMA project id: 2021.1.00393.S	J0019 + 1555	2.876	0.35	30.2	14.0
	J0104 + 1010	1.162	0.42	27.7	13.8
	J0105 + 1942	1.234	0.50	30.7	13.1
	J0106 + 1010	1.381	0.27	55.4	14.2
	J0106-0315	1.016	0.53	27.2	14.0
	J0140-0138	1.014	0.34	27.2	14.0
	J0142 + 0257	1.794	0.28	27.2	14.2
	J0351-0613	2.648	0.27	27.2	13.8
	J0758 + 1357	1.785	0.24	62.5	15.0
	J0810 + 1209	2.892	0.39	20.2	16.7
	J0811 + 1720	1.759	0.35	30.2	16.8
	J0815 + 1540	1.190	0.28	30.7	12.2
	J0826 + 1434	2.938	0.34	29.2	14.1
	J0826 + 1635	1.186	0.30	32.8	14.6
	J0827 + 0618	1.209	0.37	29.7	14.5
	J0832 + 1823	1.179	0.43	30.7	12.1
	J0837 + 0521	1.175	0.36	27.2	15.0
	J1113 + 1022	3.086	0.26	28.7	13.4
	J1213 + 0807	1.073	0.33	27.2	13.7
	J1251 + 1143	1.030	0.42	30.7	13.5
	J1532 + 1739	1.168	0.32	29.7	13.8
	J1606 + 1735	1.161	0.44	30.7	13.9
	J2059-0643	2.560	0.24	26.2	14.3
	J2108-0630	1.254	0.63	25.7	15.7
	J2239-0047	2.399	0.38	27.7	14.1
	J2256 + 0105	2.561	0.37	27.2	14.6
	J2256 + 0923	2.695	0.35	28.2	14.5
	J2300 + 0031	0.992	0.31	29.2	13.9
	J2314 + 1824	2.844	0.27	30.7	13.1
	J2348 + 1933	2.805	0.36	33.8	14.1
	J2352-0120	1.075	0.29	26.2	14.3
CO(3-2) archive	J0229-0402	0.974	0.39	9.576	20.0
ALMA project id: 2016.1.00798.S	J1000 + 0206	0.660	0.33	9.072	17.6
CO(3-2) archive		0.520	0.26	38.3	11.5
ALMA project id: 2013.1.01262.S	J1420 + 1603	0.320	0.20	36.3	11.5
CO(3-2) archive ALMA project id: 2017.1.01676.S	J1625 + 2646	1.941	0.28	15.6	17.4
CO(4-3) archive	J0052 + 0140	1.859	0.18	63.5	12.6
ALMA project id: 2019.1.01251.S	J1416 + 2649	2.107	0.21	143.1	12.2
13	J2121 + 0052	1.247	0.30	64.5	11.7
	J2123-0050	1.822	0.18	62.5	13.8
CO(7-6) archive ALMA project id: 2018.1.00583.S	J1006 + 0119	0.765	0.33	48.4	13.7

this paper we use the equivalent width (EW) of He II λ 1640 and the emission-line blueshift of C IV as tracers of the high-ionization broad line region. As discussed at length in Temple et al. (2023), the He II EW traces the strength of the unseen ionizing continuum at 54 eV, while the C IV blueshift provides a measure of outflowing disc-winds from the BLR. We assume here that the blueshifted C IV emission line profile is tracing an outflow along the line of sight (Leighly & Moore 2004; Richards et al. 2011). Together these emission lines trace the sub-parsec scale outflow and ionization properties, which can be correlated with the global ISM properties inferred from the ALMA data.

Using L_{3000} from our rest-frame UV data we can calculate a bolometric luminosity using a correction factor determined by the

following equation from Netzer (2019):

$$k_{\text{BOL}} = 25 \times (L_{3000}/10^{42})^{-0.2}$$
 (1)

For our sample we find correction factors in the range 2.6–4.3, and applying these gives us bolometric luminosities in the range $10^{46.4-47.5}$ erg s⁻¹.

2.3.2 Near-infrared spectra and BH masses

Every quasar in our main sample has a high-quality near-infrared spectrum from either Coatman et al. (2019) or the GNIRS Distant Quasar Survey (Matthews et al. 2021). These spectra were modelled homogeneously by Temple et al. (2024) to quantify emission-

line properties of [O III] and H β . Each spectrum was modelled using Fantasy (Ilić, Rakić & Popović 2023) to include a power-law continuum, Fe II multiplets, two Gaussian components for the broad Balmer lines, and two Gaussian components for each of the [O III] $\lambda\lambda$ 4960, 5008 lines. From these models we measure W_{80} , the 80 per cent velocity width of [O III], which is a measure of the strength of ionized gas outflows in the narrow-line region. For the objects considered here W_{80} lies in the range 1000–2400 km s⁻¹.

Using the full-width at half-maximum (FWHM) of the broad Balmer H β emission line, and L_{5100} we estimate the black hole mass of each object using the following single-epoch scaling relation derived by Shen et al. (2024):

$$log\left(\frac{M_{\rm BH,H\beta}}{M_{\odot}}\right) = log\left[\left(\frac{L_{5100, AGN}}{10^{44} \, {\rm erg s^{-1}}}\right)^{0.5} \left(\frac{\rm FWHM}{\rm km s^{-1}}\right)^{2}\right] + 0.85.$$
 (2)

3 ANALYSIS AND RESULTS

3.1 Spectral fitting

To extract the CO spectra for each quasar, we use an iterative process of analysing the emission at the expected location of the quasar and identify the spectral region that encompasses the entire line emission, from which we create a narrow-band image. The only exception for this was J1006+0119 where the detected emission was not centred in the cube (the expected location of the source). For this target we manually searched the region around the expected location and identified the emission slightly offset from the centre of the cube.

From the resulting collapsed images we derived the size of the emission by fitting the images using the IMFIT routine in CASA. The emission size, described by the major and minor axis as well as the position angle, was then used as the aperture to extract the final spectra. To confirm these apertures captured the total flux, we examined the total line intensity with an aperture of increasing radii starting from the sizes given by the IMFIT routine until the line intensity no longer increased. We confirm that in all but 2 cases, the full emission was captured. The 2 exceptions are J0014+0912 and J1251 + 0807 where the line intensity increased at increasing radii beyond the initial IMFIT aperture. Possible reasons for this could be extended diffuse emission and/or companions that are not bright enough to be confirmed. For these 2 sources we therefore take the aperture at which the line intensity flattens off and remains consistent with increasing aperture size.

We performed a rebinning such that all spectra were at $\sim50~km~s^{-1}$ resolution, with the exception of CO(7-6) which was binned to $\sim40~km~s^{-1}$ resolution. This allowed us to clearly identify the presence of any spectral lines within the data. Spectra (example shown in Fig. 2 with the remaining spectra shown in Fig. A1) that possess an emission line with velocity-integrated S/N >3 are then analysed using Gaussian profiles. Single and double Gaussians are fitted to each emission line with the double-Gaussian parametrization adopted when the reduced chi-square improves by more than 10 per cent. The resulting line-luminosities and FWHM are presented in Table 3.

For non-detections we present 3σ upper limits for the integrated line intensity. These are based on calculating the 1σ rms from the spectra over line-free regions, multiplying this by 3 to reach a 3σ upper limit for the peak flux. We then assume a line width that is equal to the median of those with detections and use this to model a Gaussian for which we can calculate the upper limits for the line intensity and line luminosity.

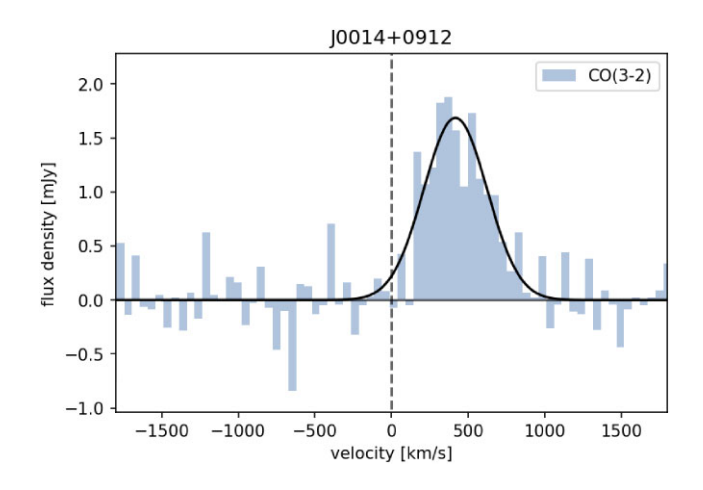


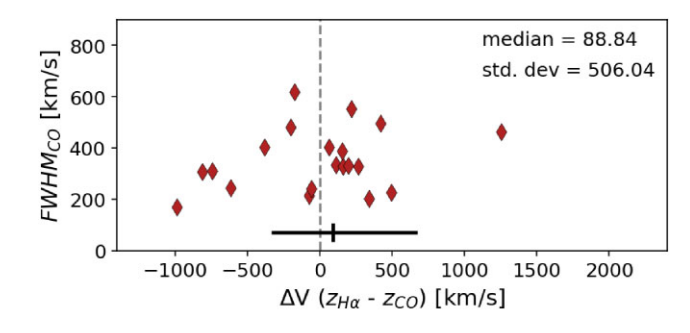
Figure 2. Example spectrum and spectral fitting for the target J0014 + 0912. We present the flux density versus velocity, in velocity bins of $50 \,\mathrm{km \, s^{-1}}$. The solid black line shows the Gaussian fit to the emission line and the dashed vertical line represents the zero velocity at the expected redshift determined from H α . The same format is used for all other spectra presented in this work (shown in Fig. A1).

We find an \sim 50 per cent detection ratio in the main sample of 32 targets which have a range of FWHM_{CO} from 170–620 km s⁻¹. Integrated line intensities for these detections range from 150 to 1900 km s⁻¹. Three of these targets are also found to have double-peaked profiles. Without spatially resolved data it is unclear as to the origin of the double peaks, which could be the result of rotation, outflows, or mergers. For BALs five out of 11 are detected and for non-BALs 14 out of 25 are detected, corresponding to 45 and 56 per cent, respectively, but given the sample size this is not statistically significant.

The archival data are reduced and analysed in the same way as the main sample. From the same analysis we find non-detections for all CO(3-2) archival data, which have rms sensitivities comparable with those of our main sample (median of 0.31 mJy compared to the main sample median of 0.345 mJy; see Table 1). However, we find detections for all 4 targets with CO(4-3) data and also the one target with CO(7-6), all of which are fitted with a single Gaussian. These have rms sensitivities of 0.195 mJy (median) and 0.33 mJy, respectively.

3.2 CO versus H α and UV redshifts

For those quasars with CO detections we were able to measure the CO redshifts and compare them to the redshifts obtained from both the rest-frame optical (from a joint fit to the broad H α and H β lines, from NIR data in Temple et al. 2024) and the rest-frame UV spectra (derived from the SDSS spectrum, as described above in Section 2.2). [O III] would provide a better estimate of the redshifts than H α , however, in the sample several of the quasars were weak or undetected in [O III] and so H α was used as an alternative to be consistent across the sample. The CO redshifts are determined from the V_{50} of CO line detection (the median velocity of the overall emission-line profile), which are mostly consistent with the H α and UV redshift determinations. The velocity offsets compared to the H α and UV redshifts are presented in Fig. 3 where we present the individual points as well as the distribution of these data, showing that there is a closer match between the H α line velocities and those of the CO(3-2), compared to what is found from the rest frame UV. With a H α measurement, it can be seen that the maximum



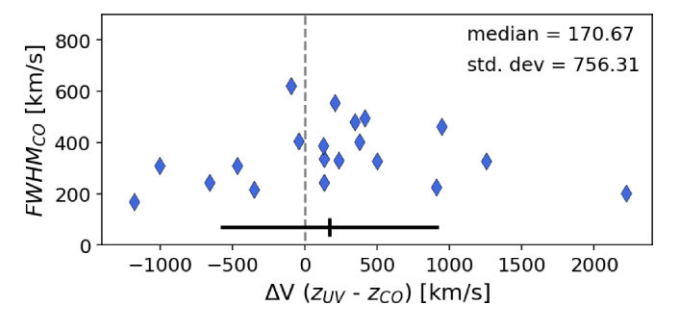


Figure 3. Figure showing the velocity offsets between the CO redshift and the H α redshift (top panel) and UV redshift (bottom panel). These are plotted against the FWHM_{CO}.

differences are $\sim 1000~\rm km~s^{-1}$, meaning that observations targeting a CO transition based on a H α redshift would still likely remain within the spectral setup with ALMA, despite the scatter. With the UV spectra from SDSS there is more scatter, with up to $2000~\rm km~s^{-1}$ offsets found. The majority of our CO redshifts agree well with the UV and optical redshifts, mostly within a few hundred km s $^{-1}$ which is the typical uncertainty at these redshifts. The robustness of our rest-UV and rest-optical redshift estimates means we are confident that the CO line would be present in the ALMA spectral window for all non-detections, which therefore allows us to derive meaningful upper limits.

3.3 Dynamical masses

The dynamical masses are calculated using the following equation, utilizing the FWHM of the CO line and assuming ordered circular rotation:

$$M_{\rm dyn} = 1.16 \times 10^5 \times 0.75 \times {\rm FWHM_{CO}} \times sin(i)^2 \times r_{kpc}$$
 (3)

and assuming that the dark matter fraction is negligible and following the same method as was used for the WISSH survey (Bischetti et al. 2021), also see Wang et al. (2013) and Venemans et al. (2016). We use i=30 degrees as the average inclination assumed for these Type 1 quasars (Mountrichas et al. 2021). We use $r_{\rm kpc}=5$ kpc based on CO size measurements from CASA when fitted using the IMFIT routine. Only three targets were spatially resolved and therefore have reliable size measurements. The sizes ranged between 0.53 and 0.65 arcsec, with an average of 0.6 arcsec, corresponding to 5 kpc at these redshifts. We therefore assume 5 kpc for all targets in the sample when calculating the dynamical masses. We discuss in Section 4.1 the effect that this assumption has on the resulting gas fractions and gas masses and the differences obtained if using sizes of 2 kpc (as seen in Bischetti et al. 2019; D'Amato et al. 2020) in calculating the dynamical mass.

In Fig. 4, we present the dynamical mass versus the black hole mass in comparison to other samples of quasars within the literature.

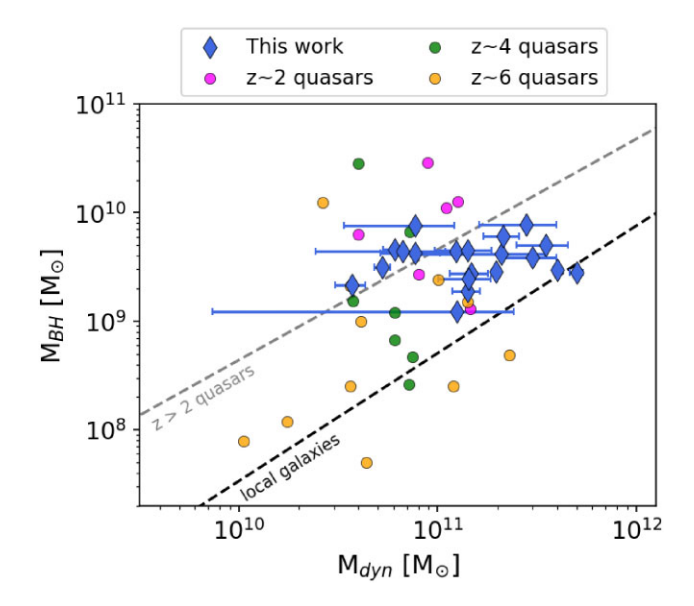


Figure 4. $M_{\rm dyn}$ versus $M_{\rm BH}$ for all our targets with detections along with others from the literature. This includes quasars at $z\sim2$ from Bongiorno et al. (2014), Banerji et al. (2015, 2017), and Brusa et al. (2018) and luminous $z\sim4$ –6 QSOs from Mortlock et al. (2011), Willott, Omont & Bergeron (2013), De Rosa et al. (2014), Kashikawa et al. (2015), Kimball et al. (2015), Willott, Bergeron & Omont (2015), Venemans et al. (2016), Trakhtenbrot et al. (2017), Venemans et al. (2017), willott, Bergeron & Omont (2017), and Feruglio et al. (2018) all of which are also collated in Pensabene et al. (2020). The dashed black line represents the local relation inferred from local galaxies (Kormendy & Ho 2013). The grey dashed line is the relation found by Pensabene et al. (2020) for a sample of quasars at z>2.

We find that for this sample, the black holes are overmassive relative to the dynamical masses. The main reason may well be as a result of selection effects, since in this work we are selecting the most luminous quasars at these redshifts (see Fig. 1). However, the results are consistent with the z>2 relation identified in Pensabene et al. (2021). Likewise, overmassive black holes were identified in similarly luminous quasars in the WISSH survey (Bischetti et al. 2021).

3.4 Gas masses and gas fractions

To calculate the gas masses we first need to calculate the line brightness temperature, $L'_{CO}[\text{K km s}^{-1}\text{pc}^2]$ using the following equation from Solomon & Vanden Bout (2005):

$$L'_{CO} = 3.25 \times 10^7 I_{CO} \nu_{CO,obs}^{-2} D_L^2 (1+z)^{-3}$$
 (4)

in units of K km s⁻¹ pc², where $v_{\text{CO,rest}}$ is the rest frequency of the CO line in GHz, D_{L} is the luminosity distance in Mpc, z is the redshift, and I is the velocity-integrated line intensity measured in Jy km s⁻¹.

We then need to convert the CO(3-2) line luminosity to the CO(1-0) line luminosity and do so assuming a line ratio of $r_{31} = 0.97$ (Carilli & Walter 2013) which is applied in the following equation:

$$L'_{\text{CO}(1-0)} = \frac{L'_{\text{CO}(3-2)}}{r_{31}}. (5)$$

For those sources with a different CO transitions we use the following line ratios: $r_{41} = 0.87$ and $r_{71} = 0.2$. These line ratio values were selected based on previous works studying similarly luminous quasars in the literature (Bothwell et al. 2013; Carilli & Walter 2013; Molyneux et al. 2024).

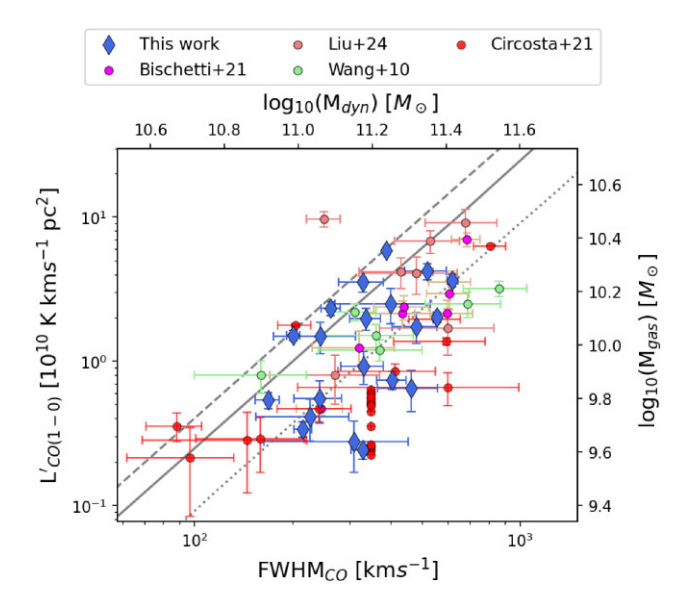


Figure 5. Here we present the FWHM_{CO} versus the CO luminosity for all targets within our sample with detections. These properties trace the dynamical mass and the gas mass, respectively. We plot other quasars and AGNs taken from the literature (Wang et al. 2010; Bischetti et al. 2021; Circosta et al. 2021; Liu et al. 2024). The solid line corresponds to the approximate best-fitting quadratic relationship for submillimeter galaxies from Bothwell et al. (2013) (as also presented in Liu et al. 2024). The dashed and dotted lines represent relations assuming spherical and disc models, respectively, Liu et al. (2024).

From the CO(1-0) line luminosity we calculate the gas mass M_{gas} , using the following equation:

$$M_{\rm gas} = \alpha_{\rm CO} \times L'_{\rm CO(1-0)},\tag{6}$$

where we use $\alpha_{CO} = 0.8 \text{ M}_{\odot}/(\text{K km s}^{-1} \text{ pc}^2)$ (Downes & Solomon 1998; Bolatto et al. 2013).

To calculate the stellar mass we use the following equation (adopted by Nguyen et al. 2020 and Bischetti et al. 2021 among others):

$$M_{\star} = M_{\rm dyn} - M_{\rm BH} - M_{\rm gas},\tag{7}$$

where the black hole mass is derived using $log(L_{5100})$ and FWHM_{Balmer} (measured from NIR spectral modelling in Temple et al. 2024, and H β black hole mass scaling relation from Shen et al. 2024). Using the stellar mass and the gas mass we can calculate a gas fraction, f_{gas} , using:

$$f_{\rm gas} = M_{\rm gas}/M_{\star} \tag{8}$$

Within our sample we find gas fractions ranging from 0.02 to 0.32, and the values for each target can be found in Table 3. We should caveat that since the stellar mass is calculated using the gas mass (as in equation (7)), the gas fraction is dependent on the assumptions made to calculate the gas mass. However, using different line ratios and $\alpha_{\rm CO}$ to calculate the gas mass provided negative stellar masses in some cases and so the chosen values are considered reasonable assumptions.

In Fig. 5, we show the FWHM_{CO} versus the CO luminosity, which can be used as proxies for the dynamical mass and the gas mass respectively. Our findings are consistent with AGNs taken from the literature and highlights low gas fractions within our sample (discussed in detail in Section 4.1 as the dynamical masses are on average larger than the gas masses. The solid grey line represents the

best fit for luminous sub-millimetre galaxies presented in Bothwell et al. (2013) and generally lies above our quasars. We also show relations assuming a disc model (dotted line in Fig. 5) and a spherical model (dashed line in Fig. 5). These models are formed from the following equation:

$$L'_{\text{CO}(1-0)} = \frac{C(\Delta V/2.355)^2 R}{\alpha \cdot G},\tag{9}$$

where Δ *V* is the FWHM of the CO line in km s⁻¹, *R* is the radius of the CO emission region in parsecs, α is the conversion factor from $L'_{\text{CO}(1-0)}$ to solar mass in K km s⁻¹ pc², *G* is the gravitational constant, and *C* is a constant related to the kinematics of the galaxy. As done in Liu et al. (2024) we use the following parameters from Erb et al. (2006): C = 2.1, R = 5 kpc, and $\alpha = 4.6$ for a disc model; and C = 5, R = 2 kpc, and $\alpha = 1.0$ for a spherical model. We find that our quasars are mostly consistent with virial relations assuming a disc model as opposed to a spherical model.

Given these low gas fractions we performed an analysis of a stacked spectrum of all CO(3-2) detections to test for the presence of underlying broad outflow components. However no broad component was identified, suggesting that outflows are not ubiquitous in this sample.

3.5 Dust continuum

As with the analysis of the spectra (described in Section 3.1), the continuum images used here are the standard ALMA reductions. There are 18 continuum-detected sources within the sample of 41 presented here (including archival data). Within the main sample we have a 38 per cent continuum detection rate (12 out of 32 with $>3\sigma$ detection). From the archival CO(3-2) 2 out of 4 are detected. In the archival CO(4-3) data all 4 are detected in continuum (with much deeper observations). And finally in the archival CO(7-6) observation there was no continuum detection.

For those detected both in CO and in continuum, the emission was identified at consistent spatial locations. Four targets also show continuum emission not associated with the quasar. For J2123–0050, emission is identified in the continuum which is co-spatial with CO emission from companions (see Fig. A2 and discussion on companions in Section 3.7).

Five sources are found to have continuum emission at mJy levels, indicating they feature significant synchrotron emission. The median continuum flux for these sources is 2.65 mJy, all of which were observed in the CO(3-2) transition. The remaining 13 continuum-detected sources show continuum emission at a level expected as coming from the Rayleigh Jeans tail of the dust spectral energy distribution. These 13 sources were observed in both CO(3-2) and CO(4-3), and we find a median continuum flux for CO(3-2) and CO(4-3) observations of 128 μ Jy and 113 μ Jy, respectively. For CO(3-2) observations, the continuum data was taken in the frequency range 97–108 GHz. For CO(4-3) observations the continuum data taken in frequency range 141–146 GHz. Finally, for the CO(7-6) observations the target had the continuum observed at a frequency of 237 GHz.

In comparison to the literature, we find a higher continuum detection rate than the SUPER survey (5 continuum detections out of 27) which study AGNs at luminosities an order of magnitude lower than ours (Circosta et al. 2021). In literature samples with similarly luminous quasars (but at higher redshifts) such as the WISSH survey (Bischetti et al. 2021), a higher continuum detection rate is found with an 80 per cent detection rate, but similar continuum fluxes to our sample having a median of 0.25 mJy. Further, in a sample of Hot Dust-

Obscured Galaxies (HotDOGs), again at similar luminosities and redshift, they find a higher detection rate, with 9 out of 13 detections (Sun et al. 2024). They have a median continuum flux of 144μ Jy for CO(3-2) detections, and so are slightly brighter in continuum in comparison to our sample, which is expected for luminous dust-obscured quasars. For those with CO(4-3) detections in Sun et al. (2024), the median continuum flux is $212 \ \mu$ Jy, between 93 and 140 GHz, consistent with our CO(3-2) and CO(4-3) measurements.

We looked for correlations between the dust continuum properties of the quasars and their CO properties and found no significant dependencies. There were no differences in C IV blueshift, [O III] W_{80} and Eddington ratio between continuum-detected and non-detected sources. Likewise, no difference in rest-frame UV or CO properties was found between quasars showing mJy level flux in the continuum and those showing μ Jy level flux. All continuum flux densities are summarized in Table 3.

3.6 Connecting the rest-frame UV quasar emission to the molecular ISM $\,$

In this Section, we investigate potential correlations between the global molecular gas properties (traced by CO) and the properties of the ionized gas in the BLR (traced by C IV and He II) and in the NLR (traced by [O III]), in this sample of high-luminosity, massive quasars. Previous works have identified a relation between outflow velocities in the quasar NLR and BLR, with [O III] line widths correlating with C IV blueshift (Vietri et al. 2018; Coatman et al. 2019; Vietri et al. 2020; Temple et al. 2024) and so here we test whether a similar trend is observed in the molecular ISM. We use only the main sample with CO(3-2) data, since they were observed to a uniform sensitivity and will therefore avoid any biases relating to the different observation setups. In our analysis we split the main sample into sub-samples based on the following properties: BH mass, Eddington ratio, C IV blueshift, He II EW, [O III] W_{80} , and BALs versus non-BALS. The specific values at which we split the sample are justified below.

Since the BLR/NLR outflow properties depend on both BH mass and Eddington ratio (Temple et al. 2023, 2024), we first split the sample roughly in half based on these two quantities, corresponding to $M_{BH} = 10^{9.46}$ and $L/L_{Edd} = 0.5$ (see top 2 panels in Fig. 6). We confirm that there is no dependence of the gas fraction on BH mass and Eddington ratio. It should also be noted that the exact threshold values of BH mass and Eddington ratio chosen do not significantly change these distributions, which strengthens the evidence of no correlation to the gas fractions. Having accounted for any potential dependence of the gas fraction on the BH mass and accretion rate, we can then test for differences in gas fraction between quasars with and without strong BLR winds corresponding to a C IV blueshift threshold of 1000 km s⁻¹ (Temple et al. 2023). He II EW is anticorrelated with C IV, so quasars with C IV blueshifts $> 1000 \text{ km s}^{-1}$ have weak He II lines with EW < 1.5 Å (Rankine et al. 2020; Temple et al. 2023). Splitting the sample at these values also evenly splits the population in the C_{IV} blueshift – equivalent width parameter space (Richards et al. 2011; Rivera et al. 2022). For [O III], a W_{80} of 1750 km s⁻¹ represents the median for the sample in Temple et al. (2024).

After splitting the sample using these values, we analyse the distribution of gas fractions in each sub-sample to identify any differences. The distributions are presented by violin plots in Fig. 6 and included within the distributions are 3σ upper limits for the non-detections (however removing these does not significantly alter the results). Based on the distributions there appears to be slight differences in the gas fractions based on the rest frame UV properties of the quasars. Quasars with higher C IV blueshifts and softer ionizing

SEDs as traced by low EW He II emission seem to show a tendency to have higher gas fractions. The sub-samples of He II EW > 1.5 Å and C IV blueshift < 1000 km s $^{-1}$ are made up of 100 and 55 per cent non-detections respectively, which strengthens our tentative results. Given these are 3σ upper limits the gas fraction distributions in these sub-samples would be expected to be even lower, enhancing the differences. However, it should be noted that the differences currently are not statistically significant based on a two-sided Kolmogorov–Smirnov test (KS test), with p-values of 0.06 (for C IV blueshift and He II EW), where a value less than 0.05 is statistically significant. Nonetheless there are tentative signs of a dependence that would need investigating further with a wider sample to confirm. The remaining distributions, separating quasars based on other accretion and outflow properties (see Fig. 6), show no statistical differences in their gas fractions when analysed with a KS test.

We must caution that with the number of sources analysed here it is hard to make robust conclusions, however we might be observing a fundamental link between the SED/accretion properties that is driving trends in the observed gas fractions. Quasars with stronger disk winds and softer ionizing SEDs may preferentially be found in gas-rich host galaxies but more studies and statistical results are needed to confirm whether any correlation is real.

3.7 No strong evidence for overdensities

By analysing the presence of companions to the quasars in our sample, we can assess whether they are residing in overdense regions, which may suggest a larger supply of gas for fuelling AGNs/quasar/galaxy growth. We identify companions that are clearly present within the same spectral window as the expected CO(3-2) frequency and that are offset spatially to the quasar. The field of view for the observations covers a diameter of 80 arcsec, corresponding to a physical distance of 670 kpc at $z\sim2$, consistent with the searching radius with ALMiner (described in Section 2.2). Within the main sample of 32 quasars we identify three quasars with potential companions detected with SNR $>3\sigma$ (J0104+1010, J1606+16735, and J2256 + 0105) and within the archival sample another three quasars show evidence of companions (see cutouts in Fig. A3).

Since identifying companions was not the main focus of this paper we did not perform a search for companions outside of the spectral window in which the CO was present. We therefore cannot rule out further companions with larger velocity offsets to the target quasar.

For the targets with archival data J0052 + 0104 has a companion which is 5 times brighter in CO(4-3) than itself, and is located \sim 240 kpc from the quasar. However, it should be noted that this detection was identified on the edge of the primary beam of the observations and so should be treated with some caution due to increased noise at the edge of the ALMA observations. J1416 + 2649 has at least two companions which are located at distances \sim 30 and 75 kpc from the quasar. J2123-0050 also shows two companions which are both comparably bright to the quasar and at distances of \sim 60 projected kpc from the quasar. The emission is both blue and redshifted either side of the quasar so this could also potentially be emission expelled from the host rather than companions. For more information on each of these individual targets see Li et al. (2023).

4 DISCUSSION

Here, we discuss our findings and interpretation of the results as well as putting them into context of the wider literature. In Section 4.1, we discuss our gas fraction measurements and how

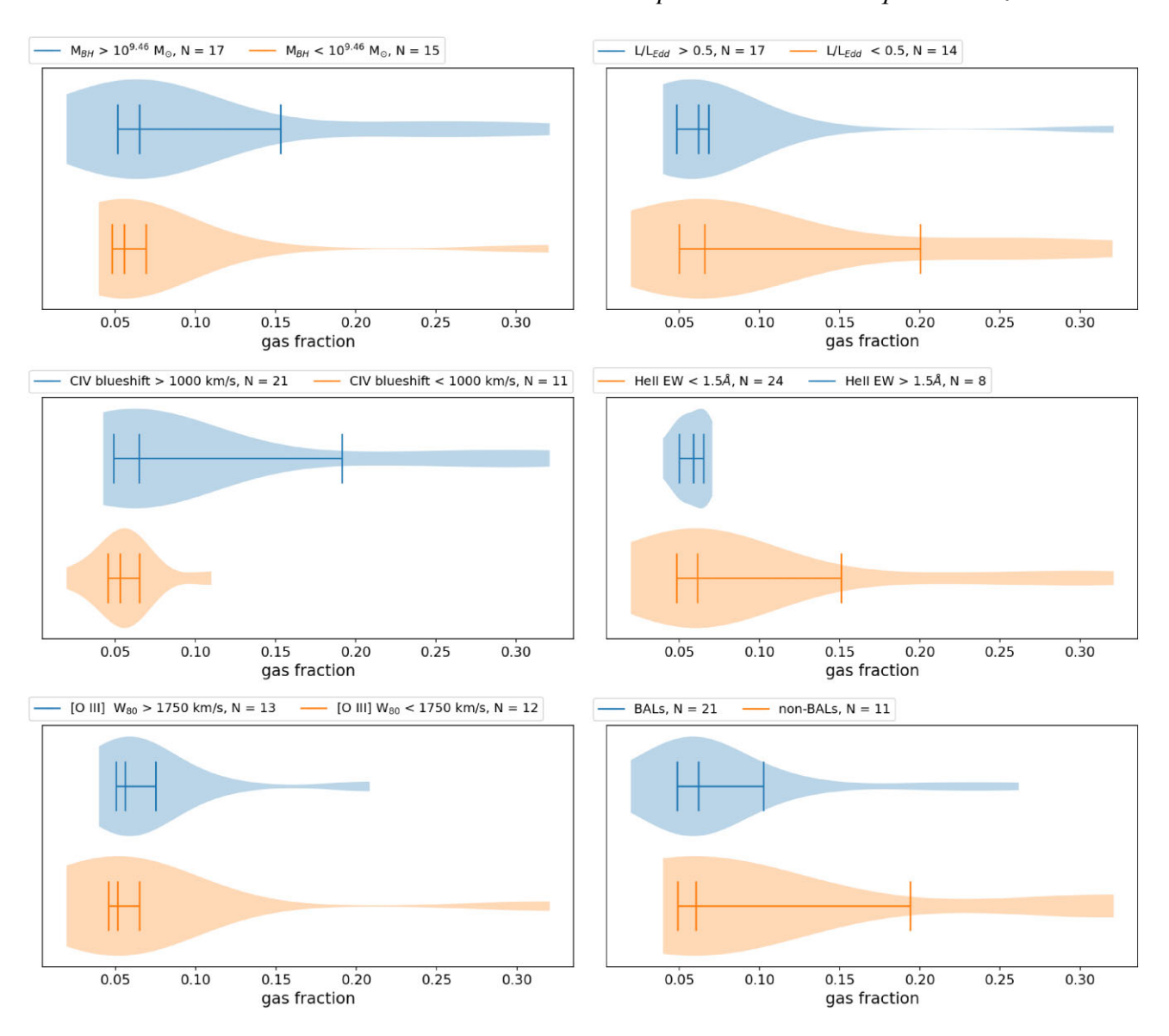


Figure 6. Violin plots to show the distribution of gas fractions when splitting the sample by different UV/optical properties. The middle solid vertical lines represent the median of the distributions and the outer 2 vertical lines show 16th and 84th quartiles. The larger regions show the full distributions from minimum to maximum values. The wider the shaded region, the more data lie within that region. *Top row:* Splitting the sample by black hole mass of 10^{9.46} M_☉ (left) and by Eddington ratio = 0.5 (right). *Middle row:* Splitting the sample by C IV blueshift = 1000 km s⁻¹ (left), and He II EW = 1.5 Å (right). *Bottom row:* Split by [O III] $W_{80} = 1750$ km s⁻¹ (left) and by BALs versus non-BALs (right). In all cases 'N' is the number of sources within each distribution. Note that 3σ upper limits are also included here for those with non-detections.

they compare to literature samples across redshifts. In Section 4.2, we discuss evidence for different gas fractions in obscured versus unobscured quasars. Finally, in Section 4.3 we present a discussion about companions identified in the sample.

4.1 Gas depletion in luminous Type 1 quasars at cosmic noon

As shown in Fig. 7, we present gas fractions for our sample alongside other samples of quasars, AGNs and star-forming galaxies (SFGs) taken from the literature across the redshift range 0–5. For this analysis, we have assumed that each survey/presented work has chosen the most sensible values of α_{CO} and line ratios based on their knowledge of their own samples. The different assumptions of line ratios and α_{CO} for each literature sample can be found in Table 2. We identify similar gas fractions in our sample to the findings of

the WISSH survey, which are similarly luminous quasars at z > 2 (Bischetti et al. 2021). However, we find lower gas fractions in our sources compared to lower luminosity quasars at the same redshift (e.g. Circosta et al. 2021) and to SFGs also at the same redshift (Sanders et al. 2023). We also find lower gas fractions when compared to a sample of HotDOGs at a slightly higher redshift (Sun et al. 2024).

Since we don't have direct stellar mass measurements and we instead derive them from the dynamical and gas masses (shown in equation (7)), we have analysed what values of α_{CO} and line ratio would be required to increase our gas fractions to the level of other studies, namely Perna et al. (2018), Circosta et al. (2021) and Sun et al. (2024). If we keep α_{CO} at 0.8 $M_{\odot}/(K \text{ km s}^{-1} \text{ pc}^2)$ we would need an r_{31} of \sim 0.1. Alternatively, fixing r_{31} at 0.97 we would need an α_{CO} of \sim 11 $M_{\odot}/(K \text{ km s}^{-1} \text{ pc}^2)$. Both values seem unlikely for luminous quasars based on the literature. If we alter both parameters

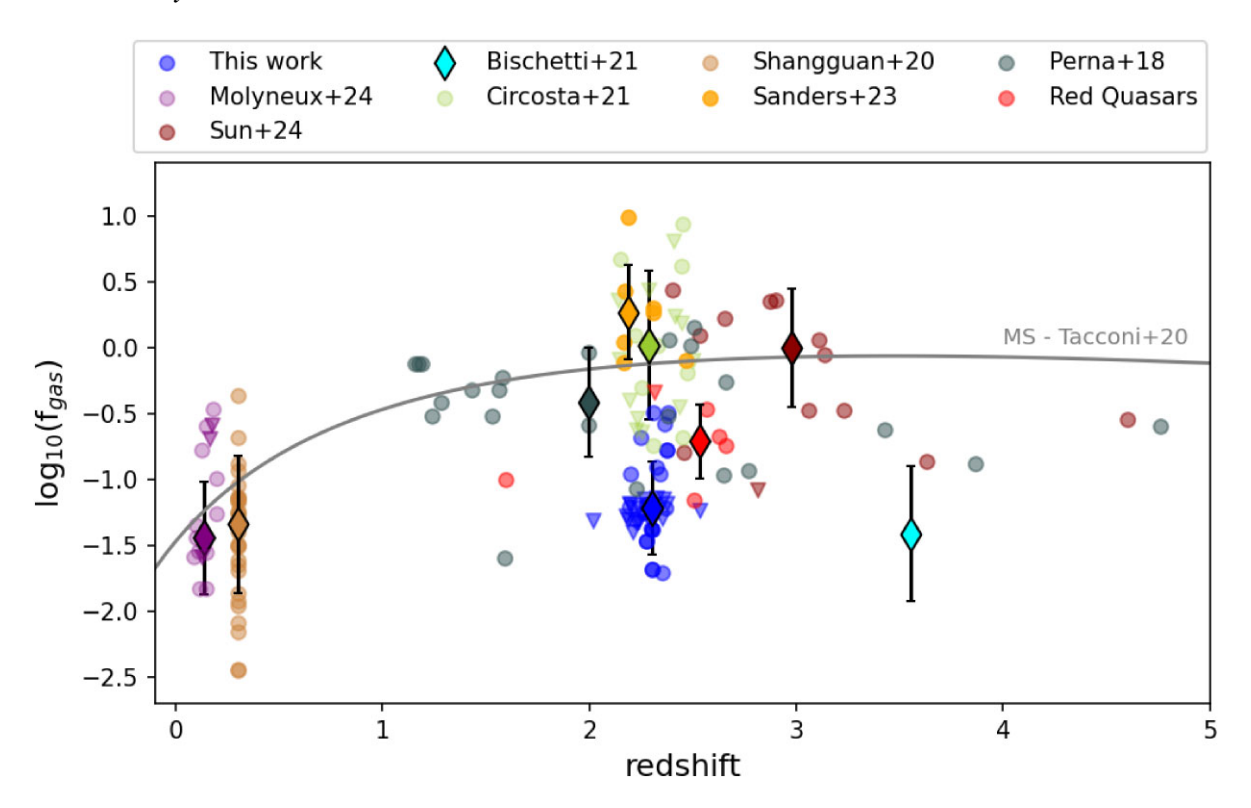


Figure 7. Figure showing the gas fractions of our sample of quasars in relation to other samples of quasars, AGNs, and star-forming galaxies up to redshifts of 5. The grey line indicates the relation for main-sequence star-forming galaxies with stellar mass $10^{11} M_{\odot}$ described in Tacconi et al. (2020). Upper limits are presented as downward triangles. For each sample presented the median redshift and gas fraction, as well as the standard deviation in gas fraction is presented as a diamond with the corresponding errorbars. Literature data taken from the following works: Banerji et al. (2017, 2018, 2021), Perna et al. (2018), Shangguan et al. (2020), Bischetti et al. (2021), Circosta et al. (2021), Sanders et al. (2023), Molyneux et al. (2024), and Sun et al. (2024).

Table 2. Table summarizing the literature samples shown in Fig. 7 including type of object, redshift of the sample, bolometric luminosities, sensitivity of the observations as well as the α_{CO} and line ratios used in those studies. Literature studies from the following works: Perna et al. (2018), Lamperti et al. (2020), Shangguan et al. (2020), Bischetti et al. (2021), Circosta et al. (2021), Sanders et al. (2023), Molyneux et al. (2024), and Sun et al. (2024). Red Quasars are a compilation from Feruglio et al. (2014), Brusa et al. (2015), and Banerji et al. (2017, 2018, 2021). Line sensitivity quoted is for the upper CO transition, estimate taken from ALMA archive (or equivalent if not ALMA) to be consistent across all samples. Those with \dagger are measured values as opposed to assumed values.

Sample	Туре	Redshift	$\begin{array}{c} log(L_{bol}) \\ (erg \ s^{-1}) \end{array}$	$\alpha_{\rm CO}$ M_{\odot} /(K km s ⁻¹ pc ²)	Line ratio	Line sensitivity, $\Delta v = 10 \text{ km s}^{-1}$ (mJy/beam)	Beam size (arcsec)
This work	Quasars	2.0-2.6	46.4–47.5	0.8	$r_{31} = 0.97$ $r_{41} = 0.87$ $r_{71} = 0.20$	0.47-0.77	0.5–3.0
Sun + 24	Hot DOGs	2.2-4.6	47.1-47.9	0.8	$r_{31} = 0.97$	0.39-1.40	0.3-1.0
Bischetti + 21	Quasars	2.4–4.7	47.2–48.0	0.8	$r_{41} = 0.87$ $r_{51} = 0.69$	0.38–1.27	0.2-5.0
Red Quasars	Quasars	1.5 - 2.7	46.8-48.5	0.8	$r_{31} = 1$		0.8 - 1.0
Perna + 18	Quasars	1.2–4.8	43.9–47.6	0.8–3.6	$r_{21} = 0.8-1$ $r_{31} = 0.1-1$ $r_{41} = 0.41-1$	0.17–2.61	
Molyneux + 24	Quasars	0.1-0.2	45.7-46.8	4	$r_{31} = 0.77^{\ +0.31}_{\ -0.20}^{\ +0}$	0.73-2.76	4.3-32.5
Shangguan + 20	PG Quasars	0.02-0.1	44.7-46.0	3.1	$r_{21} = 0.62$	3.57-5.36	6.0-8.0
Circosta + 21	AGN	2.1-2.4	44.7-46.9	3.6	$r_{31} = 0.5$	0.46-1.28	0.8 - 1.7
Sanders + 23	SFGs	2.0-2.5		$0.6615.22^{\dagger}$	$r_{31} = 0.55$		0.7-2.5

at the same time, we can match the gas fractions of our sample to the HotDOGs and SUPER sample using an α_{CO} of 4.6 $M_{\odot}/(K \text{ km s}^{-1} \text{ pc}^2)$ and an r_{31} of 0.4. Again, these values would seem unlikely given these are luminous quasars and that similarly luminous quasars in the literature are expected to have values of $r_{31}=1$ and

 $\alpha_{CO}=0.8~M_{\odot}/(K~km~s^{-1}~pc^2).$ We conclude that we are therefore indeed seeing depleted gas reservoirs compared to these literature samples.

An important factor to consider in the gas masses, and therefore gas fractions, are the assumed sizes used to calculate the dynamical

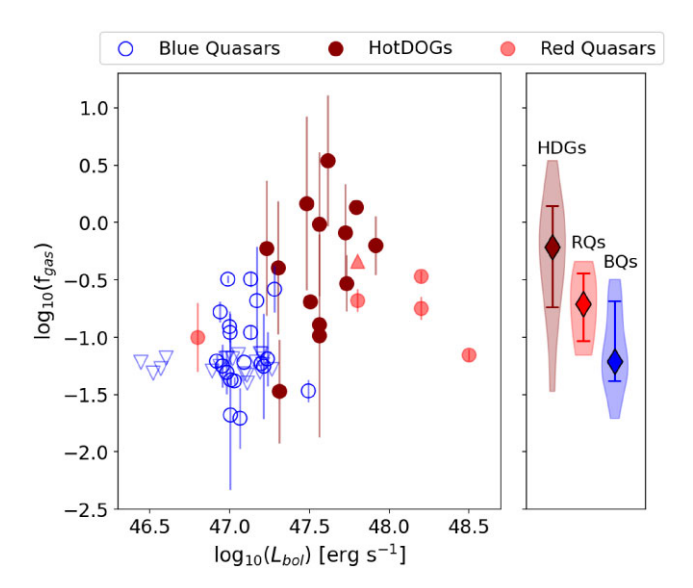


Figure 8. Gas fraction versus bolometric luminosity. Here, we focus on the AGNs and quasars above z=2 and with $L_{\rm bol}>10^{46.5}$ erg s⁻¹. Open circles and triangles are unobscured, filled circles and triangles are obscured/red quasars. For all samples presented here we calculate the gas fractions using the same $\alpha_{\rm CO}$ and line ratio for consistency. Blue quasars are data from this work. HotDOGs are data from Sun et al. (2024) and red quasars are compiled from Feruglio et al. (2014), Brusa et al. (2015), Banerji et al. (2017, 2018, 2021), and Stepney et al. (2024).

masses. As stated in Section 3.4, we assume 5 kpc sizes since those which are resolved from the beam have these measured sizes. Molecular gas at 5 kpc has been identified but as outflows and not part of the main bulk rotation. However, commonly quasars at these redshifts are found with sizes closer to 2 kpc (Bischetti et al. 2019; D'Amato et al. 2020). If assuming 2 kpc sizes, the median $\log_{10}(f_{\rm gas})$ would be -0.76 ± 0.34 compared to -1.22 ± 0.27 when assuming r=5 kpc. The overall result of depleted gas reservoirs in luminous quasars would therefore not change but the difference in gas fractions compared to the main sequence of star-forming galaxies would not be as large.

Cosmological simulations such as SIMBA, EAGLE, and IllustrisTNG suggest that AGN host galaxies at $z \sim 2$ should match or exceed non-active galaxies in gas fraction (Ward et al. 2022), which is the opposite of the observed trend. These simulations don't probe AGNs and quasars with luminosities greater than $L_{\rm bol} = 10^{45}$ erg s⁻¹ which are the luminosity of our quasars. For further discussion on the differences between simulations and observations see Bertola et al. (2024).

4.2 Gas fractions in obscured versus unobscured quasars

In Fig. 8 we compare the gas fractions in our sample of unobscured, blue quasars with luminous, obscured quasars above z=2 such as HotDOGs (Sun et al. 2024) and red quasars (Banerji et al. 2017, 2018, 2021). We find lower gas fractions in our sample compared to both red quasars and HotDoGs, but with significant overlap between the samples. The HotDOGs have very high gas column densities (Ricci et al. 2017; Vito et al. 2018; Assef et al. 2020), which could suggest that they are in an earlier evolutionary phase compared to our unobscured quasars.

These results support the picture of dusty and red quasars, going through a 'blow-out' phase and evacuating the obscuring gas in the nuclear region, leaving more depleted gas reservoirs in the resulting blue quasars (e.g. Banerji et al. 2012; Temple et al. 2019; Lansbury et al. 2020; Calistro Rivera et al. 2021). In this picture, accretion exceeding the effective Eddington limit (due to the high fuel supply as a gas rich galaxy) is followed by an expulsion of material leading to a red quasar phase and finally an unobscured quasar phase. Recent observational results of red quasars may provide evidence of this blow-out phase, showing that molecules can survive in high velocity outflows even in quasars with $L_{\rm AGN} > 10^{48}$ erg s⁻¹ (Stacey et al. 2022). Such outflows are also predicted by simulations where radiation pressure on dust can launch outflows at galactic scales (Costa et al. 2018a, b).

Overall, for this sample of luminous unobscured quasars, we conclude that we are observing host galaxies with lower gas fractions in comparison to similarly luminous obscured quasars at similar redshifts.

4.3 Companions to luminous quasars at $z \sim 2$

Within the main sample of this work, with sensitivities down to $\sim 0.5 \text{mJy}$ per 33 km s $^{-1}$ bin width, we find a few examples for CO-emitting companions to the quasars but no strong evidence that this is ubiquitous. As mentioned in Section 3.7, three targets show strong evidence for companions – J0104+1010, J1606+1735, and J2256+0105. If there are companions for the other targets it would suggest that they are all less luminous than the detected quasars at these frequencies (rest frame frequency in the range $\sim 103-108~\text{GHz}$).

The only other targets within the full sample of quasars presented here which have companions are those with archival CO(4-3) observations. These observations reached sensitivities ~ 2 times better than for our sample (see Table 1). These companions were first presented in Li et al. (2023). Out of the 10 quasars presented in Li et al. (2023), 7 had companions. It should be noted that the measured luminosities of the companions in these cases are mostly comparable to the observed quasar, and in only 1 of the 7 cases is the luminosity of the quasar much brighter than the companion(s). However, the CO(4-3) luminosities of the quasars in the sample of Li et al. (2023) are significantly lower than the CO(3-2) luminosities in our sample, with a median of 4.4×10^9 K km s⁻¹ pc² compared to 17.5×10^9 K km s⁻¹ pc², respectively (see Table 3 for the values for individual quasars).

In similarly luminous quasars to ours from the WISSH survey at z>2, 80 per cent of the quasars were identified as residing in high density environments, with the sample showing line emitting companions at distances between 6 and 130 kpc from the quasar (Bischetti et al. 2021). Within the literature there are many other examples of quasar systems with overdensities detected (e.g. Banerji et al. 2017, 2018; Díaz-Santos et al. 2018; Fogasy et al. 2020; Lambert et al. 2024; Zewdie et al. 2024). These also include samples of quasars with intense ongoing star formation (SFR > 1000 M_{\odot} per year). Spectroscopically identified companions to luminous quasars are found up to redshifts of 6 (e.g. Decarli et al. 2017; Trakhtenbrot et al. 2017). Companions have also been found to be as bright as the quasar host galaxies themselves indicating that these galaxies and quasars are residing in dense, gas rich environments (Neeleman et al. 2019).

We can also look to simulations to provide context on the predictions that luminous quasars should reside in overdensities.

Table 3. CO line properties: (1) SDSS source name. (2) CO transition used. a indicates CO(3-2) from SUPER survey Circosta et al. (2021) and b , c from ALMA projects 2013.1.01262.S and 2017.1.01676.S, respectively, not the main CO(3-2) sample here. (3) CO redshift determined from the V_{50} and corresponding uncertainty. (4) line intensity. (5) FWHM of CO line and corresponding uncertainty. (6) CO line luminosity (brightness temperature) for the specific CO transition observed. (7) Gas mass, derived from the CO line luminosity and assuming line ratios of $r_{31} = 0.97$, $r_{41} = 0.87$, and $r_{71} = 0.2$, and $\alpha_{CO} = 0.8 \text{ M}_{\odot}/(\text{K km s}^{-1} \text{ pc}^2)$. (8) Gas fraction (ratio of gas mass to stellar mass). (9) Dust continuum.

Source	CO line	z _{CO}	Line intensity [mJy km s ⁻¹]	FWHM _{CO} [km s ⁻¹]	L'_{CO} [1 × 10 ⁹ × K km s ⁻¹ pc ²]	$log(M_{gas})$ $[M\odot)]$	Gas fraction	S _{cont} [mJy]
(1)	(2)	(3)	(4)	(5)	(6)	(7)	(8)	(9)
J0014 + 0912	CO(3-2)	2.3478 ± 0.0003	1460 ± 186	518 ± 76	42.31 ± 5.38	10.54 ± 0.05	0.11 ± 0.04	< 0.03
J0019 + 1555	CO(3-2)	_	< 367	_	< 10.49	< 9.92	< 0.07	0.50 ± 0.03
J0052 + 0140	CO(4-3)	2.3104 ± 0.0001	205 ± 25	215 ± 13	3.25 ± 0.39	9.49 ± 0.05	0.06 ± 0.01	0.11 ± 0.02
J0104 + 1010	CO(3-2)	2.3634 ± 0.0002	291 ± 66	262 ± 18	8.53 ± 1.93	9.83 ± 0.05	0.06 ± 0.06	0.27 ± 0.03
J0105 + 1942	CO(3-2)	2.3232 ± 0.0002	667 ± 113	336 ± 37	18.99 ± 3.22	10.20 ± 0.07	0.12 ± 0.04	< 0.05
J0106 + 1010	CO(3-2)	_	< 279	_	< 8.45	< 9.83	< 0.05	< 0.02
J0106-0315	CO(3-2)	2.2412 ± 0.0003	533 ± 131	243 ± 69	14.25 ± 3.50	10.08 ± 0.10	0.21 ± 0.16	83.7 ± 1.60
J0140-0138	CO(3-2)	_	< 358	_	< 9.99	< 9.90	< 0.06	< 0.03
J0142 + 0257	CO(3-2)	_	< 295	_	< 8.71	< 9.84	< 0.52	1.64 ± 0.03
J0229-0402	$CO(3-2)^a$	_	< 405	_	< 10.88	< 9.94	< 0.07	1.97 ± 0.04
J0351-0613	CO(3-2)	_	< 283	_	< 7.80	< 9.80	< 0.05	0.59 ± 0.02
J0758 + 1357	CO(3-2)	_	< 246	_	< 6.69	< 9.73	< 0.04	2.65 ± 0.04
J0810 + 1209	CO(3-2)	_	< 406	_	< 11.59	< 9.97	< 0.07	< 0.03
J0811 + 1720	CO(3-2)	_	< 367	_	< 10.93	< 9.94	< 0.07	< 0.05
J0815 + 1540	CO(3-2)	_	< 288	_	< 8.01	< 9.81	< 0.05	< 0.04
J0826 + 1434	CO(3-2)	_	< 356	_	< 10.50	< 9.92	< 0.06	2.71 ± 0.04
J0826 + 1635	CO(3-2)	_	< 309	_	< 8.29	< 9.82	< 0.05	0.10 ± 0.02
J0827 + 0618	CO(3-2)	_	< 392	_	< 10.59	< 9.93	< 0.06	< 0.13
J0832 + 1823	CO(3-2)	2.2785 ± 0.0003	190 ± 62	242 ± 40	5.23 ± 1.71	9.64 ± 0.15	0.06 ± 0.03	< 0.03
J0837 + 0521	CO(3-2)	_	< 377	_	< 11.52	< 9.96	0.15	< 0.04
J1000 + 0206	$CO(3-2)^a$	_	< 344	_	< 9.94	< 9.90	< 0.07	< 0.05
J1006 + 0119	CO(7-6)	2.3096 ± 0.0001	451 ± 64	329 ± 26	2.33 ± 0.33	9.74 ± 0.06	0.06 ± 0.01	< 0.07
J1113 + 1022	CO(3-2)	2.2699 ± 0.0003	145 ± 46	226 ± 72	3.96 ± 1.26	9.52 ± 0.14	0.06 ± 0.04	< 0.02
J1213 + 0807	CO(3-2)	_	< 347	_	< 10.75	< 9.93	< 0.07	< 0.03
J1251 + 1143	CO(3-2)	2.2003 ± 0.0004	965 ± 262	400 ± 130	24.99 ± 6.78	10.31 ± 0.11	0.11 ± 0.08	0.09 ± 0.02
J1416 + 2649	CO(4-3)	2.2997 ± 0.0003	167 ± 65	309 ± 145	2.63 ± 1.02	9.40 ± 0.18	0.02 ± 0.02	0.41 ± 0.02
J1420 + 1603	$CO(3-2)^{b}$	_	< 269	_	< 8.18	< 9.82	< 0.05	< 0.02
J1532 + 1739	CO(3-2)	2.2006 ± 0.0006	214 ± 68	462 ± 97	5.54 ± 1.76	9.72 ± 0.14	0.02 ± 0.01	< 0.01
J1606 + 1735	CO(3-2)	_	531 ± 189	540 ± 120	15.85 ± 5.64	10.10 ± 0.16	< 0.06	< 0.01
J1625 + 2646	$CO(3-2)^{c}$	_	< 291	_	< 8.58	< 9.84	< 0.06	0.17 ± 0.03
J2059-0643	CO(3-2)	2.3327 ± 0.0001	511 ± 41	201 ± 9	14.65 ± 1.18	10.08 ± 0.04	0.32 ± 0.05	< 0.05
J2108-0630	CO(3-2)	2.3344 ± 0.0001	1154 ± 168	329 ± 52	33.13 ± 4.82	10.45 ± 0.06	0.26 ± 0.05	< 0.05
J2121 + 0052	CO(4-3)	2.3736 ± 0.0001	309 ± 39	168 ± 14	5.14 ± 0.65	9.69 ± 0.06	0.17 ± 0.03	0.06 ± 0.01
J2123-0050	CO(4-3)	2.2813 ± 0.0002	459 ± 66	404 ± 41	7.12 ± 1.02	9.83 ± 0.06	0.03 ± 0.01	0.12 ± 0.02
J2239-0047	CO(3-2)	2.2234 ± 0.00023	635 ± 155	480 ± 75	16.75 ± 4.09	10.15 ± 0.11	0.05 ± 0.02	< 0.09
J2256 + 0105	CO(3-2)	2.2716 ± 0.0003	325 ± 83	330 ± 49	8.90 ± 2.27	9.87 ± 0.11	0.06 ± 0.02	< 0.04
J2256 + 0923	CO(3-2)	2.2981 ± 0.00033	693 ± 63	554 ± 15	19.36 ± 1.76	10.20 ± 0.04	0.04 ± 0.01	< 0.05
J2300 + 0031	CO(3-2)	_	< 327	_	< 8.66	< 9.84	< 0.05	0.08 ± 0.02
J2314 + 1824	CO(3-2)	_	< 277	_	< 8.04	< 9.81	< 0.05	< 0.06
J2348 + 1933	CO(3-2)	2.1932 ± 0.0002	1345 ± 129	619 ± 24	34.63 ± 3.32	10.46 ± 0.04	0.06 ± 0.01	0.18 ± 0.03
J2352-0120	CO(3-2)	2.3826 ± 0.0001	1888 ± 83	388 ± 7	56.15 ± 2.47	10.67 ± 0.02	0.32 ± 0.02	0.12 ± 0.02
Companions								
J0104 + 1010	CO(3-2)	2.3632 ± 0.0004	337 ± 93	350 ± 112	9.88 ± 2.72	_	_	_
J1606 + 1735	CO(3-2)	2.3327 ± 0.0003	489 ± 106	517 ± 130	14.02 ± 3.04	_	_	_
J2108-0630	CO(3-2)	2.3793 ± 0.0004	236 ± 71	310 ± 108	7.02 ± 2.12	_	_	_
J2256 + 0105	CO(3-2)	2.2735 ± 0.0004	353 ± 70	486 ± 111	9.70 ± 1.90	_	_	_
J0052 + 0140	CO(4-3)	2.3097 ± 0.0002	756 ± 133	332 ± 73	11.98 ± 2.11	_	_	_
J1416 + 2649 # 1	CO(4-3)	2.2932 ± 0.0005	359 ± 62	586 ± 118	5.62 ± 0.97	-	_	_
J1416 + 2649 # 2	CO(4-3)	2.2898 ± 0.0001	83 ± 18	121 ± 31	1.30 ± 0.28	_	_	_
J2123-0050 # 1	CO(4-3)	2.2844 ± 0.0003	370 ± 50	495 ± 77	5.75 ± 0.78	_	_	_
J2123-0050 # 2	CO(4-3)	2.2778 ± 0.0003	367 ± 54	477 ± 81	5.68 ± 0.84	-	-	-

For example, GALFORM simulations predict that 33 per cent of simulated quasars at z=2.8 would have companion galaxies at distances <350 kpc (Fogasy et al. 2017, 2020). Of these simulated quasars, 2.4 per cent would be expected to have a bright companion with SFR > 100 $\rm M_{\odot}$ per year. These simulations were analysed with a time slice of \sim 200 Myr, corresponding to $\Delta z \sim$ 0.2.

The findings of our work suggests one of two things: either there are only a few cases for companions present in the main sample of quasars and therefore we find no strong evidence for overdensities. Alternatively, there are companions present but we would need to go much deeper with observations to identify them, as was done for the CO(4-3) work (Li et al. 2023).

5 CONCLUSIONS

In this work, we have presented ALMA CO observations of a sample of 41 quasars at $z\sim 2$, with 32 sources observed in CO(3-2) and 9 archival sources with either CO(3-2), CO(4-3), and CO(7-6) observations. Most of the sources are spatially unresolved with only three being marginally resolved. The observations therefore trace the global molecular ISM properties in these quasars. We compare the gas fractions of our sample to literature samples of quasars/AGNs and non-AGNs across the redshift range 0–5, as well as specifically to red quasars and HotDOGs. We compare the observed molecular gas properties to available multiwavelength data tracing ionized gas on both sub-parsec and kpc scales (C IV and [O III]). The main findings from this work are as follows:

- (i) We obtain a 47 per cent detection rate in the main sample of sources with CO(3-2) data. From the nine sources included from the ALMA archive, we find 4 non-detections in CO(3-2), 4 detections in CO(4-3), and a single detection in CO(7-6). We identify a range of CO properties and find a median gas mass of $8.0 \pm 1.5 \times 10^9 \ M_{\odot}$ and a range of FWHM_{CO} from 200 to $\sim 600 \ km \ s^{-1}$.
- (ii) Our observations of molecular gas in a large, statistically significant sample at $z\sim 2$ reveals evidence for depleted gas reservoirs in luminous, unobscured z=2 quasars with a median gas fraction of 0.06 ± 0.09 . This is compared to similarly luminous red quasars and HotDOGs in the literature with gas fractions of 0.28 ± 0.13 and 0.63 ± 0.90 , respectively. This indicates a trend of increasing gas fraction with obscuration and may support the idea of an evolutionary phase in AGNs, where quasar host galaxies move from more gas rich and obscured to gas poor and unobscured.
- (iii) We identify tentative hints at a correlation between the gas fractions and He II EW and C IV blueshifts. Quasars with C IV blueshifts > 1000 km s $^{-1}$ have gas fractions in the range 0.04–0.32 compared to those with C IV blueshifts < 1000 km s $^{-1}$ with lower gas fractions in the range 0.02–0.11. Similarly quasars with He II EW > 1.5 Å have gas fractions in the range 0.04–0.07 whereas those with He II EW < 1.5 Å have gas fractions in the range 0.02–0.32. These correlations are currently not statistically significant and larger samples are needed to test this further. High C IV blueshift quasars with softer ionizing SEDs (and therefore lower He II EW) are expected to be driving stronger disc winds in the quasar broad line region. Our results may therefore point to a link between strong BLR outflows and enhanced gas fractions in luminous quasars at cosmic noon.
- (iv) Three targets out of the main sample of 32 show signs of a companion galaxy detected in CO. ALMA archival data with deeper observations show more significant evidence for companions, with 3 out of 4 observed in CO(4-3) showing evidence for companions. This suggests that lower luminosity companions might be present across the main sample; however, we would need deeper observations to

test this further. Overall we find no strong evidence for overdensities in our sample of luminous quasars at $z \sim 2$.

ACKNOWLEDGEMENTS

SJM acknowledges funding from The Royal Society through a Research Fellows Enhancement Award Grant (RF/ERE/221053) awarded to MB. MB acknowledges funding from The Royal Society via a University Research Fellowship. MJT was supported by UKRI STFC (ST/X001075/1). CR acknowledges support from Fondecyt Regular grant 1230345, ANID BASAL project FB210003 and the China-Chile joint research fund. ALR acknowledges support from a UKRI Future Leaders Fellowship (grant code: MR/T020989/1). GCJ acknowledges support by the Science and Technology Facilities Council (STFC), by the ERC through Advanced Grant 695671 'QUENCH', and by the UKRI Frontier Research grant 'RISEand-FALL'. RJA was supported by FONDECYT grant number 1231718 and by the ANID BASAL project FB210003. MA acknowledges support from ANID Basal Project FB210003 and and ANID MILE-NIO NCN2024_112. For the purpose of open access, the author has applied a Creative Commons Attribution (CC BY) licence to any Author Accepted Manuscript version arising from this submission.

DATA AVAILABILITY

This paper makes use of the following ALMA data: ADS/JAO. ALMA\#2021.1.00393.S, ADS/JAO.ALMA\#2016.1.00798.S, ADS/JAO.ALMA\#2013.1.01262.S, ADS/JAO.ALMA\#2017.1.01 676.S, ADS/JAO.ALMA\#2019.1.01251.S, and ADS/JAO. ALMA\#2018.1.00583.S. ALMA is a partnership of ESO (representing its member states), NSF (USA) and NINS (Japan), together with NRC (Canada), NSTC and ASIAA (Taiwan), and KASI (Republic of Korea), in cooperation with the Republic of Chile. The Joint ALMA Observatory is operated by ESO, AUI/NRAO, and NAOJ.'

The data used in this work are available from the ESO Science Archive Facility (https://archive.eso.org/). The reduced data underlying this paper will be shared on reasonable request to the corresponding author.

REFERENCES

Ahmadi A., Hacar A., 2023, Astrophysics Source Code Library. record ascl:2306.025

Assef R. J. et al., 2020, ApJ, 897, 112

Banerji M., McMahon R. G., Hewett P. C., Alaghband-Zadeh S., Gonzalez-Solares E., Venemans B. P., Hawthorn M. J., 2012, MNRAS, 427, 2275

Banerji M., Alaghband-Zadeh S., Hewett P. C., McMahon R. G., 2015, MNRAS, 447, 3368

Banerji M., Carilli C. L., Jones G., Wagg J., McMahon R. G., Hewett P. C., Alaghband-Zadeh S., Feruglio C., 2017, MNRAS, 465, 4390

Banerji M., Jones G. C., Wagg J., Carilli C. L., Bisbas T. G., Hewett P. C., 2018, MNRAS, 479, 1154

Banerji M., Jones G. C., Carniani S., DeGraf C., Wagg J., 2021, MNRAS, 503, 5583

Baskin A., Laor A., Hamann F., 2013, MNRAS, 432, 1525

Baskin A., Laor A., Hamann F., 2015, MNRAS, 449, 1593

Bertola E. et al., 2024, A&A, 691, A178

Bischetti M. et al., 2019, A&A, 628, A118

Bischetti M. et al., 2019, A&A, 628, A116

Bolatto A. D., Wolfire M., Leroy A. K., 2013, ARA&A, 51, 207

Bongiorno A. et al., 2014, MNRAS, 443, 2077

Bothwell M. S. et al., 2013, MNRAS, 429, 3047

Brusa M. et al., 2015, A&A, 578, A11

Brusa M. et al., 2018, A&A, 612, A29

Calistro Rivera G. et al., 2021, A&A, 649, A102

Carilli C. L., Walter F., 2013, ARA&A, 51, 105

Carniani S. et al., 2015, A&A, 580, A102

Cicone C., Feruglio C., Maiolino R., Fiore F., Piconcelli E., Menci N., Aussel H., Sturm E., 2012, A&A, 543, A99

Circosta C. et al., 2018, A&A, 620, A82

Circosta C. et al., 2021, A&A, 646, A96

Coatman L., Hewett P. C., Banerji M., Richards G. T., Hennawi J. F., Prochaska J. X., 2019, MNRAS, 486, 5335

Concas A. et al., 2022, MNRAS, 513, 2535

Costa T., Rosdahl J., Sijacki D., Haehnelt M. G., 2018a, MNRAS, 473, 4197

Costa T., Rosdahl J., Sijacki D., Haehnelt M. G., 2018b, MNRAS, 479, 2079

Cresci G., Maiolino R., 2018, Nat. Astron., 2, 179

Cresci G. et al., 2015, ApJ, 799, 82

D'Amato Q. et al., 2020, A&A, 636, A37

De Rosa G. et al., 2014, ApJ, 790, 145

Decarli R. et al., 2017, Nature, 545, 457

Díaz-Santos T. et al., 2018, Science, 362, 1034

Downes D., Solomon P. M., 1998, ApJ, 507, 615

Erb D. K., Steidel C. C., Shapley A. E., Pettini M., Reddy N. A., Adelberger K. L., 2006, ApJ, 646, 107

Fabian A. C., 2012, ARA&A, 50, 455

Feruglio C. et al., 2014, A&A, 565, A91

Feruglio C. et al., 2015, A&A, 583, A99

Feruglio C. et al., 2018, A&A, 619, A39

Fiore F. et al., 2017, A&A, 601, A143

Fogasy J., Knudsen K. K., Lagos C. D. P., Drouart G., Gonzalez-Perez V., 2017, A&A, 597, A123

Fogasy J., Knudsen K. K., Drouart G., Lagos C. D. P., Fan L., 2020, MNRAS, 493, 3744

Harrison C. M., Alexander D. M., Mullaney J. R., Swinbank A. M., 2014, MNRAS, 441, 3306

Ilić D., Rakić N., Popović L. Č., 2023, ApJS, 267, 19

Ivison R. J. et al., 2008, MNRAS, 390, 1117

Jarvis M. E. et al., 2020, MNRAS, 498, 1560

Kakkad D. et al., 2020, A&A, 642, A147

Kashikawa N. et al., 2015, ApJ, 798, 28

Kimball A. E., Lacy M., Lonsdale C. J., Macquart J. P., 2015, MNRAS, 452, 88

Kormendy J., Ho L. C., 2013, ARA&A, 51, 511

Koss M. J. et al., 2021, ApJS, 252, 29

Lambert T. S. et al., 2024, A&A, 689, A331

Lamperti I. et al., 2020, ApJ, 889, 103

Lansbury G. B., Banerji M., Fabian A. C., Temple M. J., 2020, MNRAS, 495, 2652

Leighly K. M., Moore J. R., 2004, ApJ, 611, 107

Li J. et al., 2023, ApJ, 950, 180

Liu F.-Y. et al., 2024, ApJ, 964, 136

Longinotti A. L. et al., 2023, MNRAS, 521, 2134

Matthews B. M. et al., 2021, ApJS, 252, 15

McKee C. F., Ostriker E. C., 2007, ARA&A, 45, 565

Molyneux S. J., Harrison C. M., Jarvis M. E., 2019, A&A, 631, A132

Molyneux S. J. et al., 2024, MNRAS, 527, 4420

Mortlock D. J. et al., 2011, Nature, 474, 616

Mountrichas G., Buat V., Georgantopoulos I., Yang G., Masoura V. A., Boquien M., Burgarella D., 2021, A&A, 653, A70

Mullaney J. R., Alexander D. M., Fine S., Goulding A. D., Harrison C. M., Hickox R. C., 2013, MNRAS, 433, 622

Neeleman M. et al., 2019, ApJ, 882, 10

Netzer H., 2019, MNRAS, 488, 5185

Nguyen N. H., Lira P., Trakhtenbrot B., Netzer H., Cicone C., Maiolino R., Shemmer O., 2020, ApJ, 895, 74

Pâris I. et al., 2018, A&A, 613, A51

Pensabene A., Carniani S., Perna M., Cresci G., Decarli R., Maiolino R., Marconi A., 2020, A&A, 637, A84

Pensabene A. et al., 2021, A&A, 652, A66

Perna M. et al., 2018, A&A, 619, A90

Piotrowska J. M., Bluck A. F. L., Maiolino R., Peng Y., 2022, MNRAS, 512, 1052

Rankine A. L., Hewett P. C., Banerji M., Richards G. T., 2020, MNRAS, 492, 4553

Ricci C. et al., 2017, ApJ, 835, 105

Richards G. T. et al., 2011, AJ, 141, 167

Rivera A. B., Richards G. T., Gallagher S. C., McCaffrey T. V., Rankine A. L., Hewett P. C., Shemmer O., 2022, ApJ, 931, 154

Saintonge A. et al., 2017, ApJS, 233, 22

Salomé P., Guélin M., Downes D., Cox P., Guilloteau S., Omont A., Gavazzi R., Neri R., 2012, A&A, 545, A57

Sanders R. L. et al., 2023, ApJ, 942, 24

Scholtz J. et al., 2020, MNRAS, 492, 3194

Shangguan J., Ho L. C., Bauer F. E., Wang R., Treister E., 2020, ApJ, 899, 112

Shen Y. et al., 2024, ApJS, 272, 26

Solomon P. M., Vanden Bout P. A., 2005, ARA&A, 43, 677

Stacey H. R., Arrigoni Battaia F., 2022, MNRAS, 517, L11

Stacey H. R., Costa T., McKean J. P., Sharon C. E., Calistro Rivera G., Glikman E., van der Werf P. P., 2022, MNRAS, 517, 3377

Stepney M., Banerji M., Hewett P. C., Temple M. J., Rankine A. L., Matthews J. H., Richards G. T., 2023, MNRAS, 524, 5497

Stepney M., Banerji M., Tang S., Hewett P. C., Temple M. J., Wethers C. F., Puglisi A., Molyneux S. J., 2024, MNRAS, 533, 2948

Sun W., Fan L., Han Y., Knudsen K. K., Chen G., Zhang H.-X., 2024, ApJ, 964, 95

Tacconi L. J., Genzel R., Sternberg A., 2020, ARA&A, 58, 157

Temple M. J., Banerji M., Hewett P. C., Coatman L., Maddox N., Peroux C., 2019, MNRAS, 487, 2594

Temple M. J. et al., 2023, MNRAS, 523, 646

Temple M. J. et al., 2024, MNRAS, 532, 424

Trakhtenbrot B., Lira P., Netzer H., Cicone C., Maiolino R., Shemmer O., 2017, ApJ, 836, 8

Vayner A., Zakamska N., Wright S. A., Armus L., Murray N., Walth G., 2021, ApJ, 923, 59

Venemans B. P., Walter F., Zschaechner L., Decarli R., De Rosa G., Findlay J. R., McMahon R. G., Sutherland W. J., 2016, ApJ, 816, 37

Venemans B. P. et al., 2017, ApJ, 837, 146

Vietri G. et al., 2018, A&A, 617, A81

Vietri G. et al., 2020, A&A, 644, A175

Vito F. et al., 2014, MNRAS, 441, 1059

Vito F. et al., 2018, MNRAS, 474, 4528

Wang R. et al., 2010, ApJ, 714, 699

Wang R. et al., 2013, ApJ, 773, 44

Ward S. R., Harrison C. M., Costa T., Mainieri V., 2022, MNRAS, 514, 2936

Willott C. J., Omont A., Bergeron J., 2013, ApJ, 770, 13

Willott C. J., Bergeron J., Omont A., 2015, ApJ, 801, 123

Willott C. J., Bergeron J., Omont A., 2017, ApJ, 850, 108

Wylezalek D. et al., 2022, ApJ, 940, L7

Zewdie D. et al., 2024, A&A, 694, A121

APPENDIX

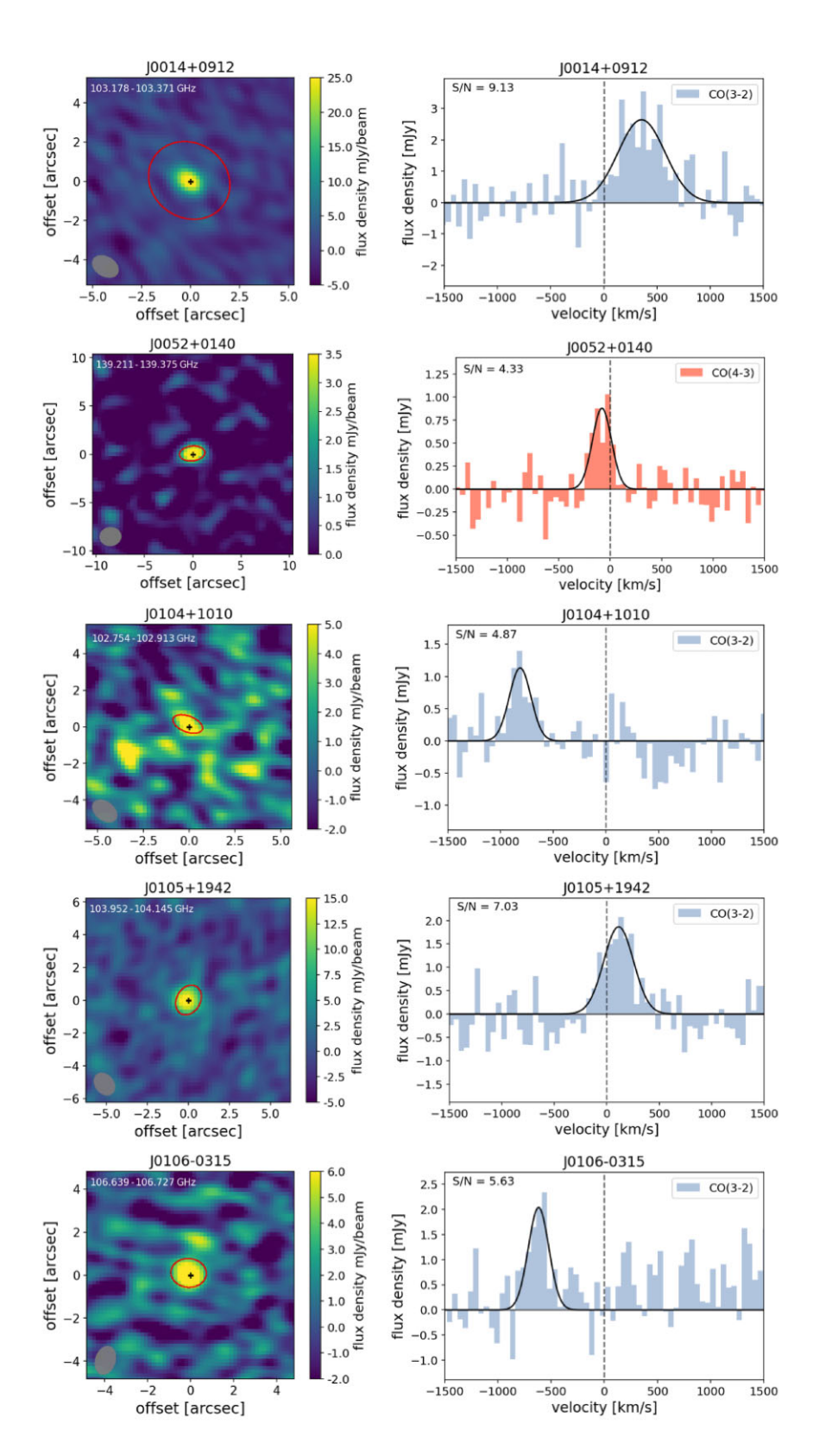


Figure A1. Left panel: Narrowband image collapsed over the frequency range indicated in the top left of the cutout. The black cross indicates the centre of the observation. The grey filled ellipse represents the corresponding beam size. The open red ellipse indicates the region where the spectrum is extracted from. The flux density in mJy/beam is indicated by the colourbar. Right panel: Spectrum extracted from the region indicated by the red ellipse in the left panel.

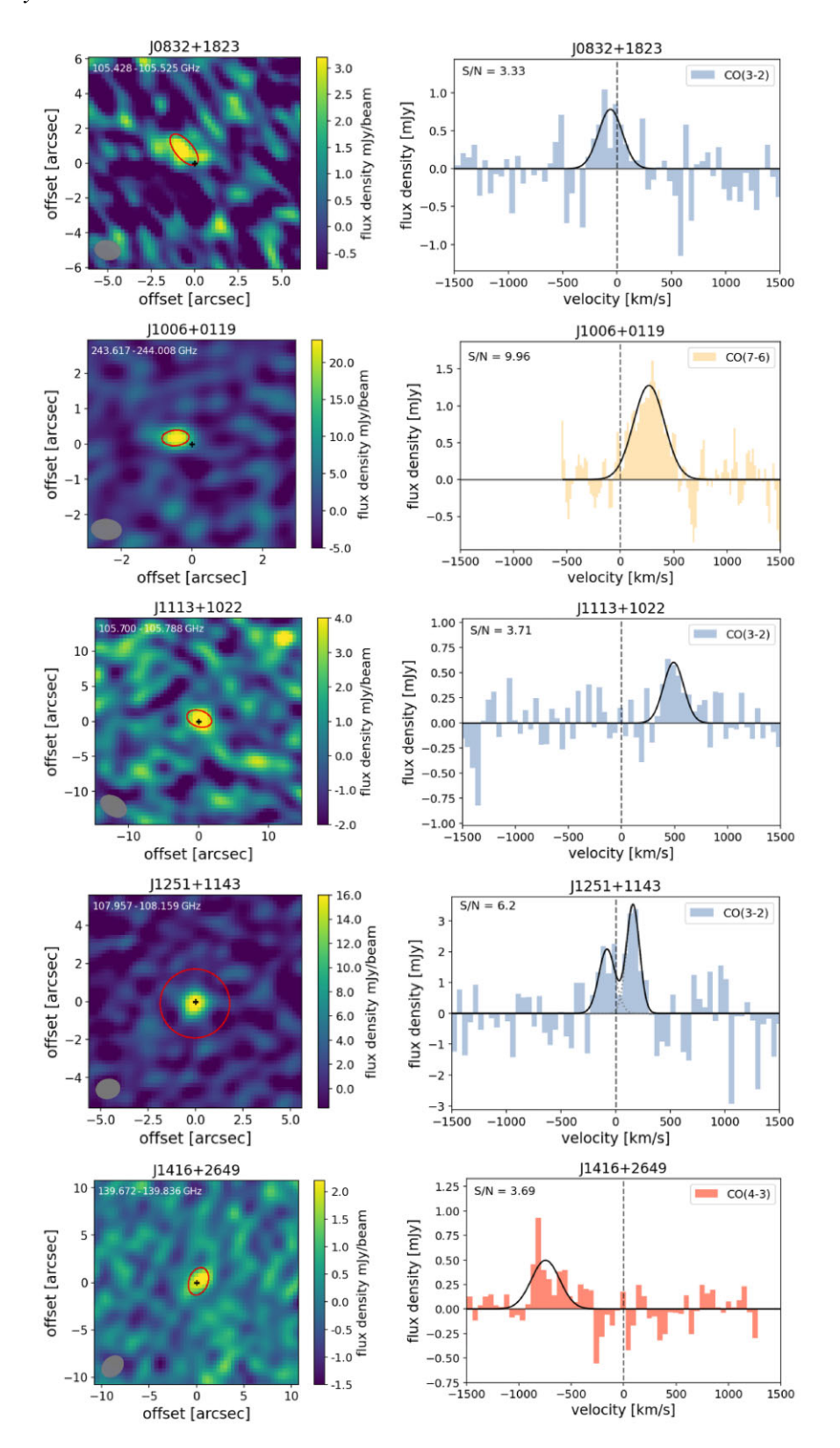


Figure A1. Continued.

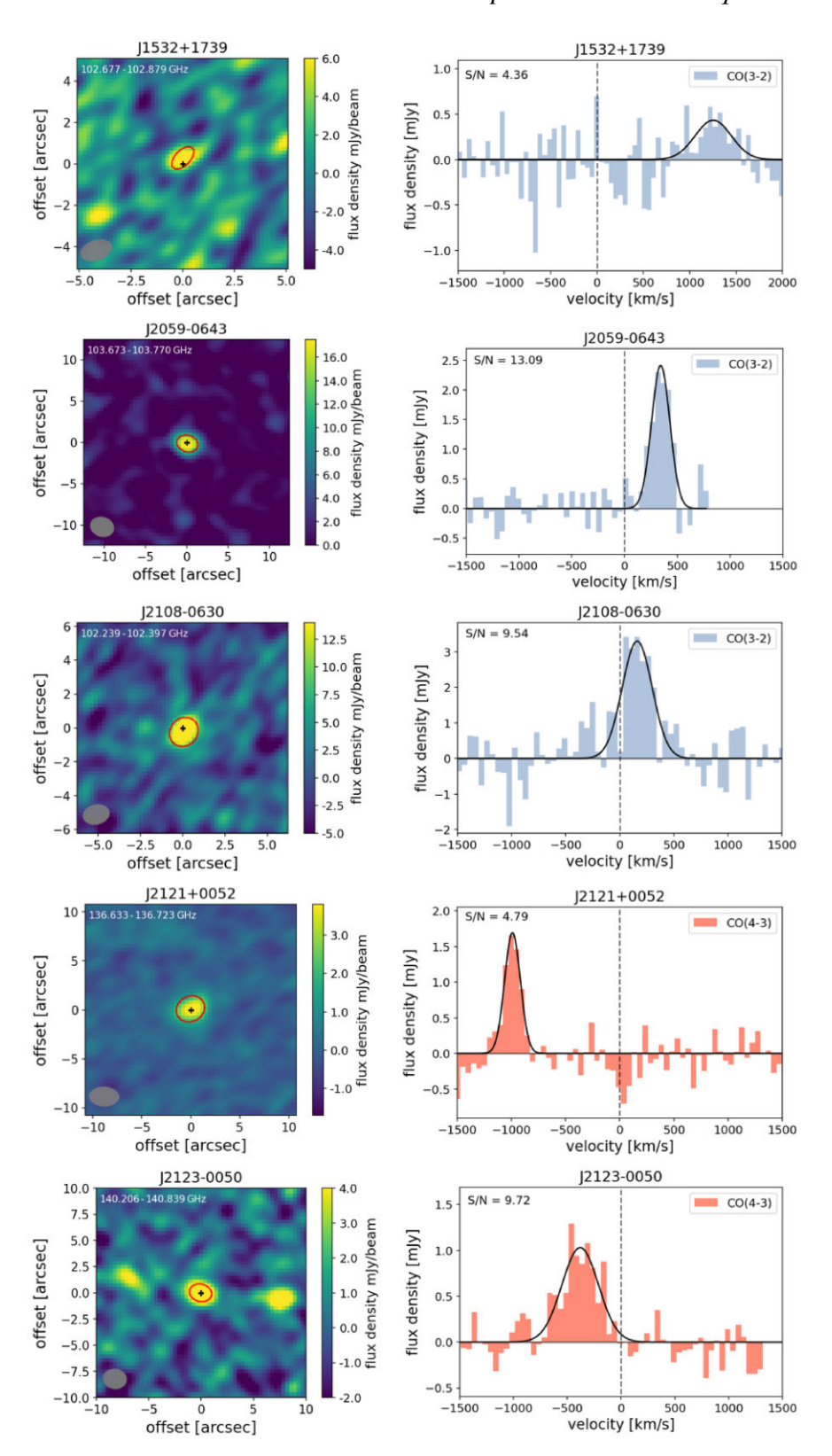


Figure A1. Continued.

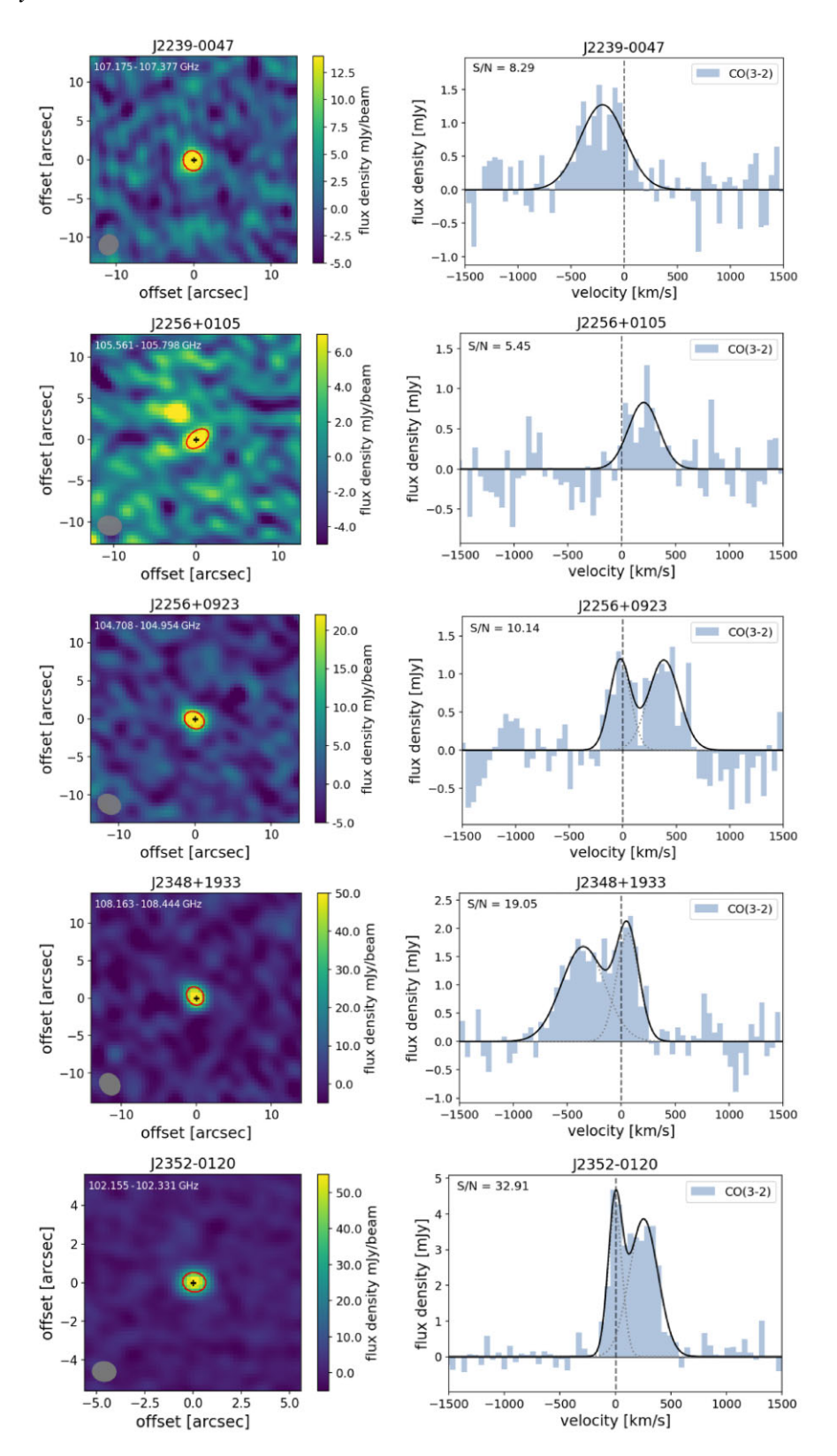


Figure A1. Continued.

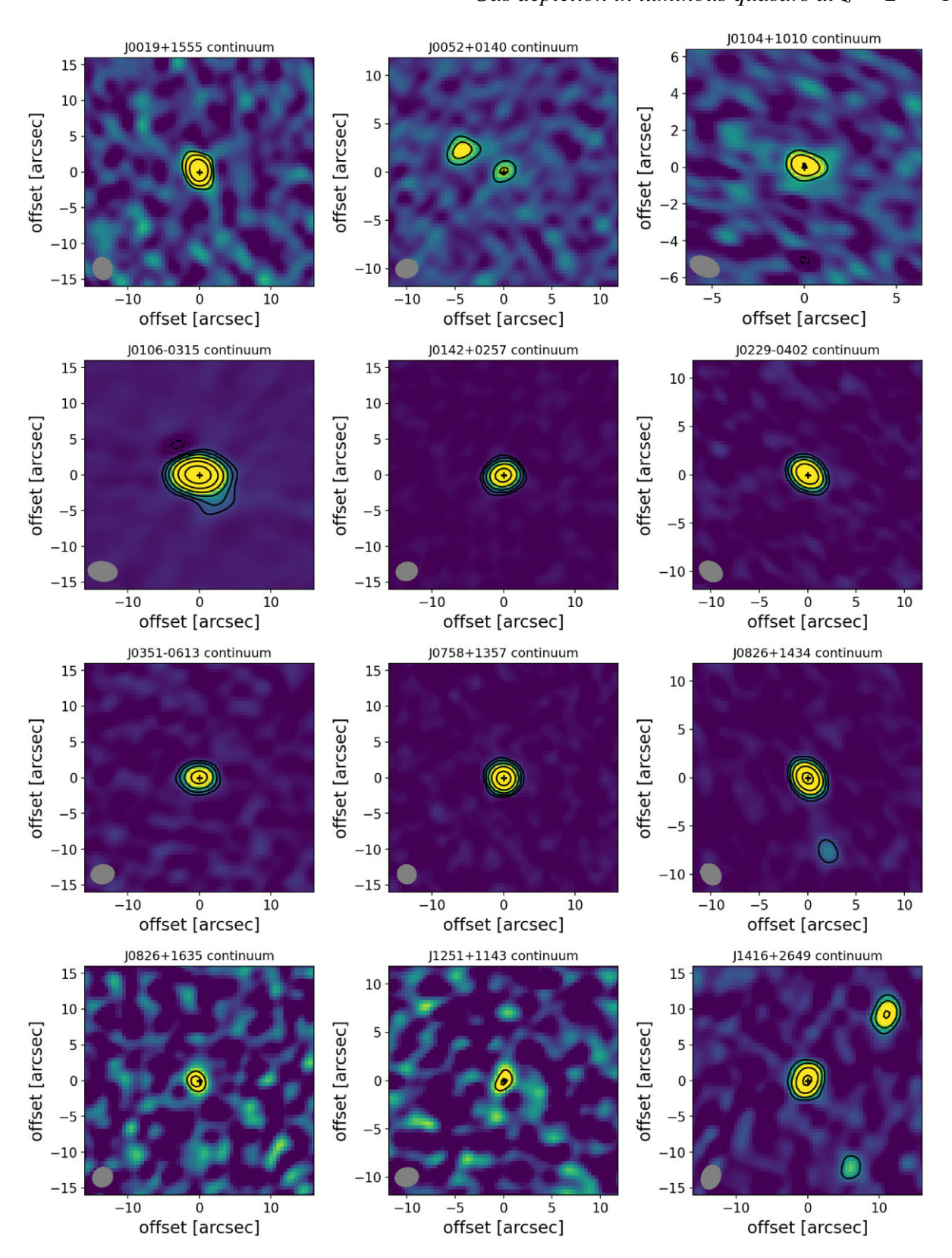


Figure A2. Continuum images for all those with continuum detections. Black crosses indicate the centre of observations. Black contours begin at 2σ . Black dashed contours correspond to negative 2σ (where present).

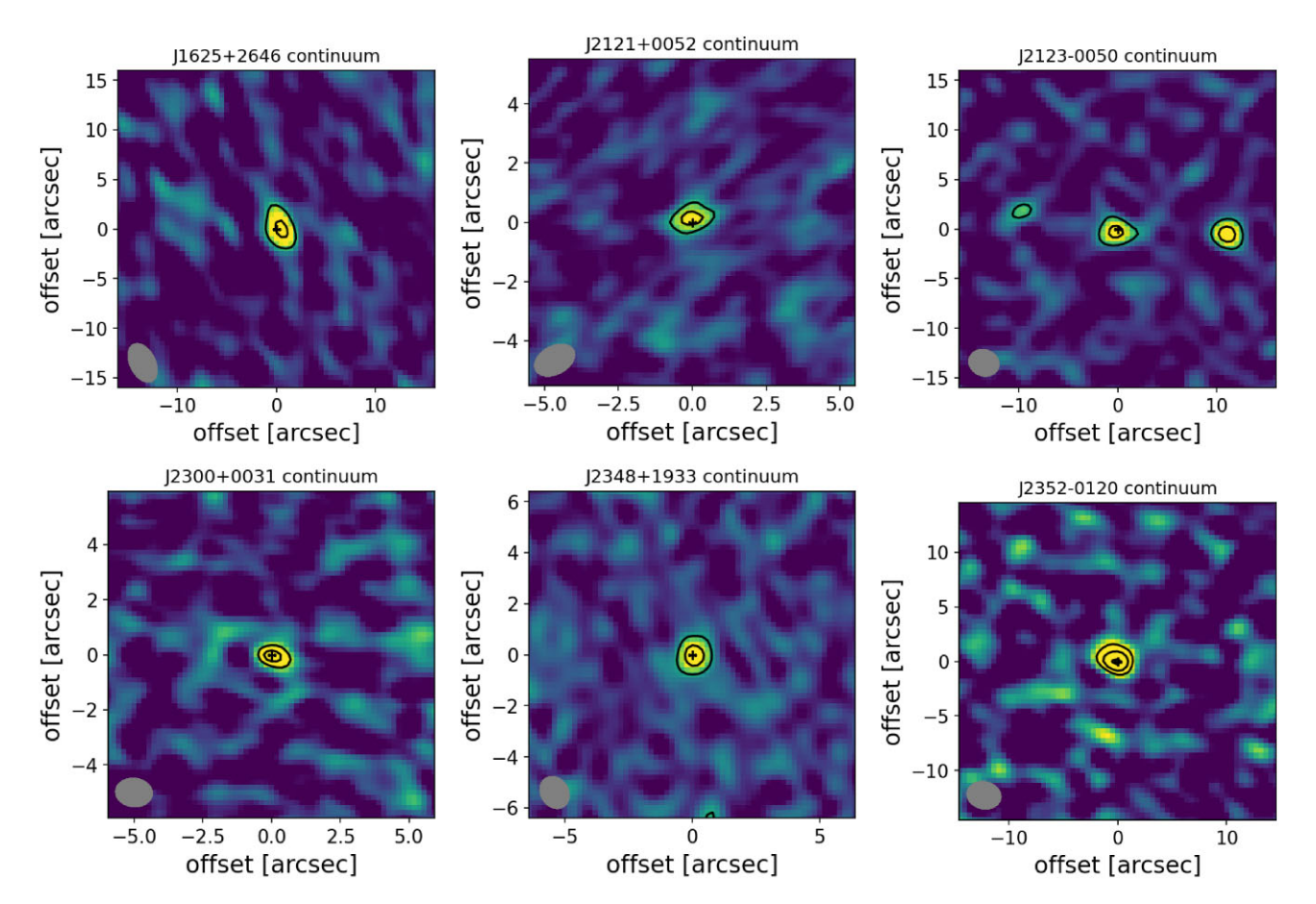


Figure A2. Continued.

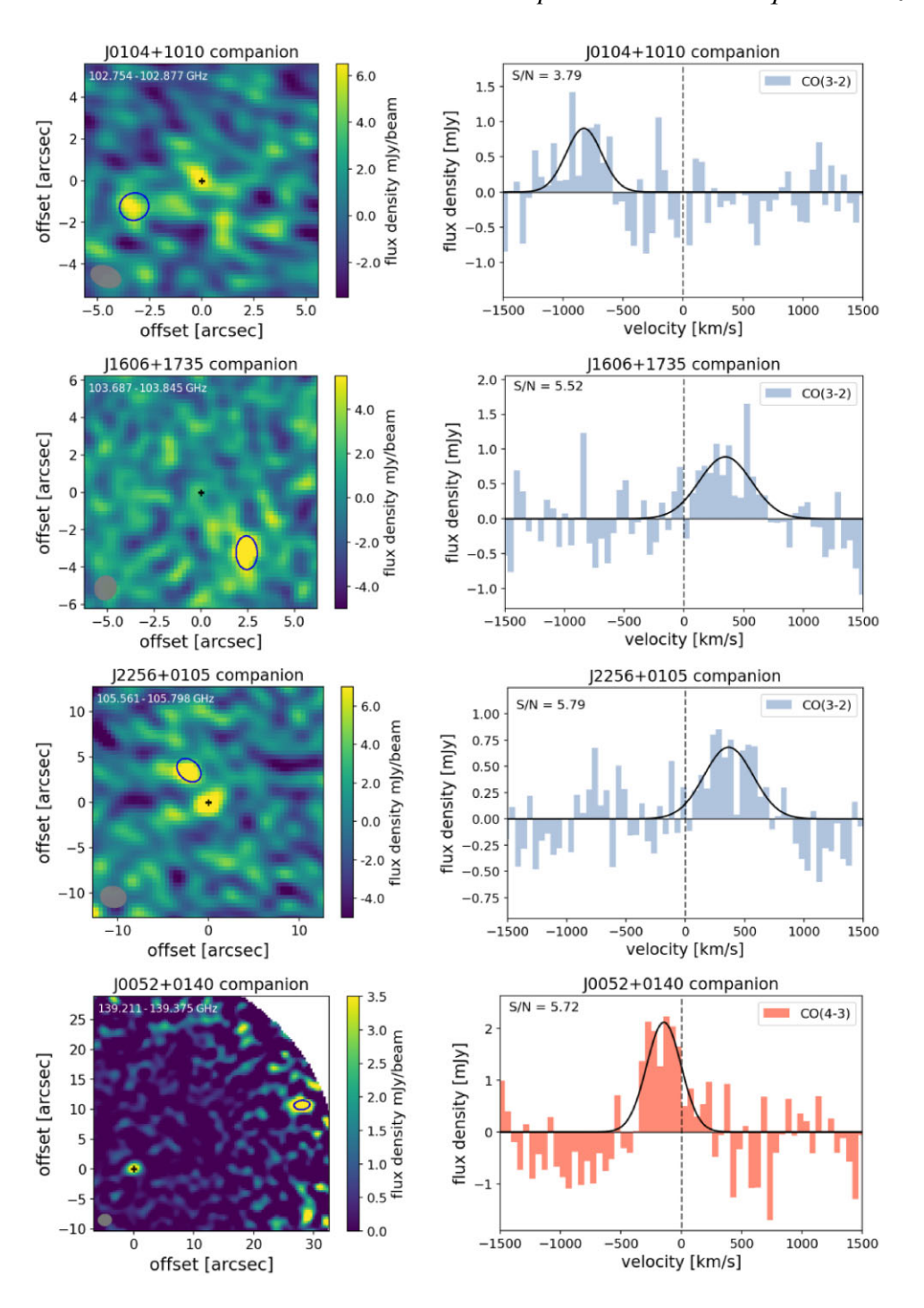


Figure A3. Spectra of companion galaxies to the quasars. Left panel: Narrowband image collapsed over the frequency range indicated in the top left of the cutout. The black cross indicates the centre of the observation. The grey filled ellipse represents the corresponding beam size. The blue open ellipse indicates the companion galaxy from which the spectrum is extracted. The flux density in mJy/beam is indicated by the colourbar. Right panel: spectrum extracted from source around the region indicated by the red ellipse in the left panel.

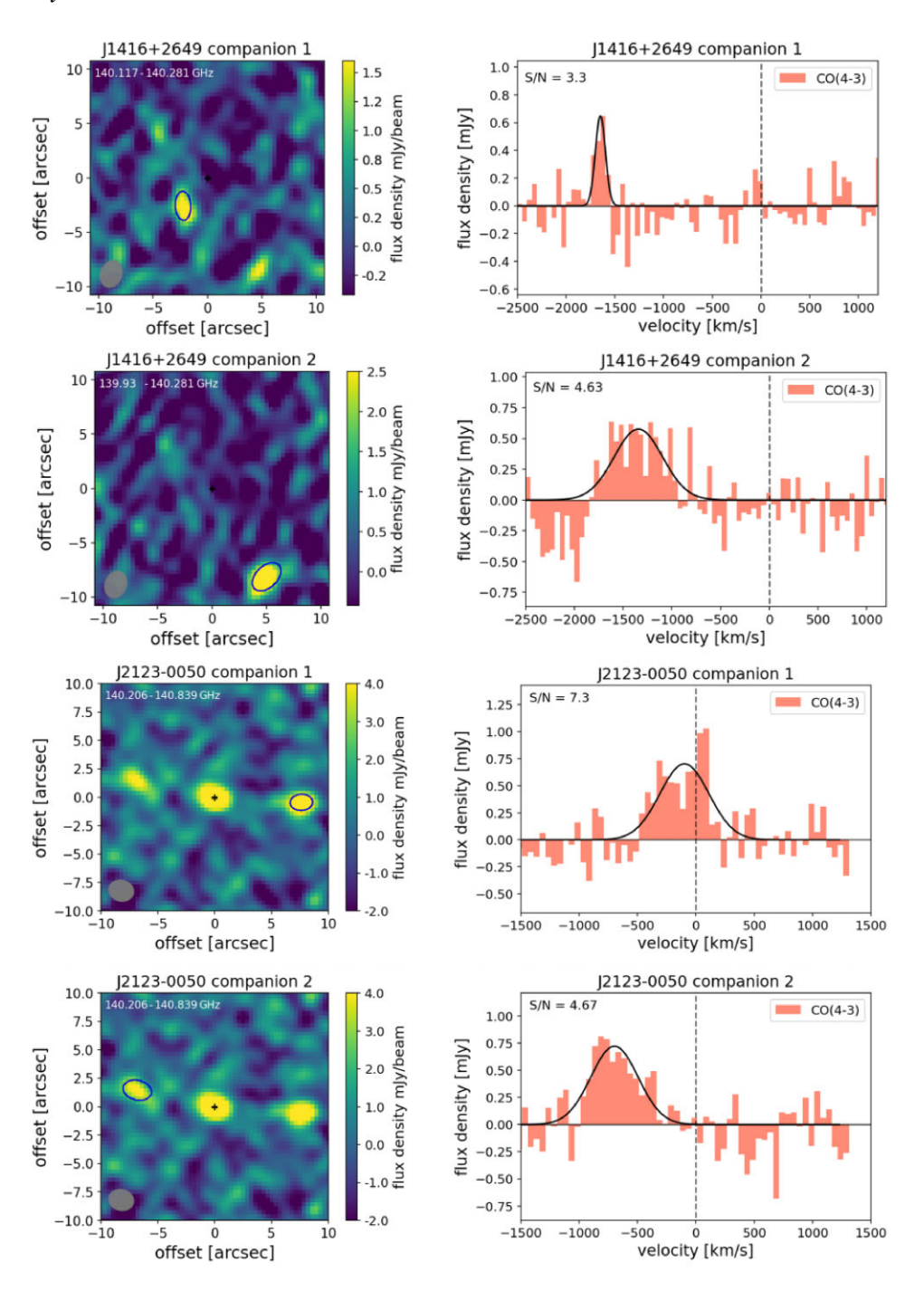


Figure A3. Continued.

This paper has been typeset from a TEX/LATEX file prepared by the author.